ORIGINAL PAPER

Ensemble-based history matching of the Edvard Grieg field using 4D seismic data

Rolf J. Lorentzen[1] · Tuhin Bhakta[1,2] · Kristian Fossum[1] · Jon André Haugen[3] · Espen Oen Lie[4] · Abel Onana Ndingwan[3] · Knut Richard Straith[3]

Abstract

The Edvard Grieg field is a highly complex and heterogeneous reservoir with an extensive fault structure and a mixture of sandstone, conglomerate, and shale. In this paper, we present a complete workflow for history matching the Edvard Grieg field using an ensemble smoother for Bayesian inference. An important aspect of the workflow is a methodology to check that the prior assumptions are suitable for assimilating the data, and procedures to verify that the posterior results are plausible and credible. We thoroughly describe several tools and visualization techniques for these purposes. Using these methods we show how to identify important parameters of the model. Furthermore, we utilize new compression methods for better handling large datasets. Simulating fluid flow and seismic response for reservoirs of this size and complexity requires high numerical resolution and accurate seismic models. We present a novel dual-model concept for a better representation of seismic data and attributes, that deploy different models for the underground depending on simulated properties. Results from history matching show that we can improve data matches for both production data and different seismic attributes. Updated parameters give new insight into the reservoir dynamics, and are calibrated to better represent water movement and pressure.

Keywords Data assimilation · Field study · Ensemble methods · Seismic modeling

Mathematics Subject Classification (2010) 62M20 · 86-10 · 86A15 · 62F15

1 Introduction

Ensemble-based assimilation of production data for large-scale models is well established. Demonstrations of ensemble-based history matching using time-lapse seismic data are however more scarce, despite the fact that seismic surveys are available for many offshore and onshore petroleum reservoirs. There are several reasons for this, such as difficult characterization of the correlated data noise, complicated seismic modeling processes, challenging prior parameter and uncertainty selection, and memory-exhaustive data volumes. Large modeling errors and poorly specified data noise, combined with limited degrees of freedom for the parameter space, lead to unsatisfactory history-matching results. An

analysis of the performance of ensemble-based assimilation is found in [8]. In that paper the ensemble smoother with multiple data assimilation (ES-MDA) method was used [9], to update a selection of reservoir properties in a heavy-oil turbidite reservoir in the Campos Basin, Brazil. Relatively successful assimilation of both production and seismic data is reported but with an underestimation of the posterior model uncertainty. There exist other applications of ES-MDA for 4D seismic history matching [e.g.,15, 25, 33], and in general, the mismatches to both seismic and production data were reduced. In [19] both production and seismic data were used to estimate a broad set of reservoir properties (porosity, permeability, water-oil-contacts, fault transmissibility multipliers, etc.) in a model for the Norne field. In that work, they used a method based on regularized Levenberg-Marquardt (RLM), solving a minimum average cost (MAC) problem, see [21]. An improvement in the data match was reported. Common for the above-mentioned works is that reservoir models of moderate sizes are considered. Quantitative utilization of large-scale data in the seismic domain therefore remains a challenge, and it remains to embed model cali-

✉ Rolf J. Lorentzen
rolo@norceresearch.no

1 NORCE Norwegian Research Centre AS, Bergen, Norway

2 Now at Equinor Energy AS, Bergen, Norway

3 Aker BP ASA, Stavanger, Norway

4 Geocore AS, Bergen, Norway

bration into a robust Bayesian workflow [12] that captures model checking and potential model improvement. For a comprehensive review of 4D seismic history matching covering different methodologies, data, and applications, see [28].

In this manuscript, we demonstrate and validate several aspects of large-scale data assimilation using big data. In particular, we investigate the use of time-lapse seismic data for calibrating a reservoir model for the Edvard Grieg field. The Edvard Grieg field is located in the North Sea in the Utsira High and is operated by Aker BP ASA. The original recoverable resources were approximately 60.4 million Sm^3, and the production started in 2015. The field is produced with pressure support from water injectors, and the reservoir produces undersaturated oil, captured in sandstone and conglomerate with varying quality. Ensemble-based assimilation of seismic and production data for the Edvard Grieg field has not been presented before, and an important contribution of this paper is a demonstration of the workflow and results for this field. We focus on all aspects of the workflow, including prior model creation, model calibration, and model checking and improvement. Significant improvements in seismic modeling, including the use of models at different scales, are presented. Unlike other applications, we utilize a seismic model that also provides credible noise estimates. In addition to seismic attributes, we use all available well and repeat formation tester (RFT) data for assimilation. To our knowledge, both the model and datasets are considerably larger than other published works on ensemble-based data assimilation for real fields. The reservoir models consist of more than 1.5 million active grid cells, and the seismic data is modeled in the seismic domain (Cartesian grids) consisting of almost 200 million data values (for each seismic cube). We apply data compression based on the (in-house) wavelet techniques introduced in [22], but the compression methodology introduced there is extended to also include information in the simulated data. Data assimilation is performed using an iterative ensemble smoother introduced in [5]. This ensemble randomized maximum likelihood method (EnRML) searches for the minimum of the objective functions using an ensemble-based approximation of the Levenberg-Marquard method. It does not rely on a predefined number of assimilation steps and differs in that sense from the ES-MDA. The computer code used for this study is based on the Python Ensemble Toolbox (PET) [26].

Parameterization and prior model creation are major challenges in the history-matching workflow. Often improvements are necessary if the calibrated models are not trustworthy or lack physical realism. In this study, we introduce several tools for prior and posterior model checking. Analysis of the model's ability to match historical data is based on the Mahalanobis measure [27], as well as novel techniques for visualizing simulated coverage of spatially dense seismic data [17]. We also introduce and demonstrate tools for assess-

ing the credibility of the updated reservoir properties, as well as tools for identifying important drivers among the vast and different types of data. We go through several examples that illustrate the importance of various parameter types, with particular focus on their ability to tune the modeled response of the seismic signals.

Successful assessment of complex and large reservoir resources benefits from diverse input from different disciplines. The outcome of an automated history-matching workflow, based on large models and big datasets, is a valuable source of information that improves reservoir management. The models used in this study have a coarse horizontal resolution compared to the vertical resolution, and assigning realistic properties is a challenge. It is not possible to capture all physical details with a numerical model, and it is important to find plausible representations of the reservoir and flow properties that give the best possible match to the measurements. The outline of the paper is as follows: In Section 2 we give a brief introduction to the Edvard Grieg field, in Section 3 we present the flow and the seismic models, and in Section 4 we present the methodology for Bayesian inversion. The results are shown in Section 5. Two types of seismic attributes are considered: amplitude maps (Section 5.2) and impedance cubes (Section 5.3). The data are based on acquisition from three seismic surveys (conducted in 2016, 2018, and 2020) using Ocean Bottom Cables (OBC). We generated one dataset based on the difference between the 2016 base survey and the 2018 monitor survey, and one dataset based on the difference between the 2018 monitor survey and the 2020 monitor survey. We assimilate seismic attributes and production data simultaneously. The production data consists of flow rates, bottom hole pressures, and RFT data. The conclusions are given in Section 6.

2 Edvard Grieg field

The Edvard Grieg oil field is located in block 16/1 in the North Sea approximately 180 km west of Stavanger, Norway, and was discovered with well 16/1-8 by Lundin Norway AS in 2007. Production start-up of the field was in November 2015 and is now operated by Aker BP ASA (Operator) and its partners OMV Norge AS and Wintershall Dea Norge AS. The field is currently producing light oil from 13 producers located mainly in the central, southern, and eastern parts of the field. To maintain the field's pressure and voidage, water is injected from three injectors in the west and one injector in the southeast corner of the Edvard Grieg field.

The reservoir geology on Edvard Grieg is complex with a wide range of unique facies of different geological ages. The main reservoir can be found in an alluvial succession which is dominated by generally poor north-derived fan deposits in the eastern and south-eastern parts of the field, while the

western and south-western parts are dominated by surrounding fan fringing deposits, also called plain deposits, see Fig. 1. These plain deposits include lacustrine shales, fluvial sandstones, and a substantial package of high-porosity aeolian sandstones. In addition, in areas between alluvial fans and aeolian sediments depositions are reworked and re-deposited by fluvial processes. The alluvial fan conglomerates found on Edvard Grieg show a large variability between producible conglomerates (found in 16/1-8) to almost non-reservoir conglomerates as seen in 16/1-10. The main difference between these conglomerates is the composition of the matrix which ranges from clean sandstones to muddy sandstones with very low permeability. The latter is often referred to as conglomerates with silty matrix, while conglomerates with cleaner sandstone matrix are referred to as conglomerates with sandy matrix. Also, as the clasts often are generally of granitic material and do not contribute to the net, clast-supported conglomerates are of poorer reservoir quality than matrix-supported conglomerates. To the north on the Tellus high, the alluvial succession is not present, leaving us with high porosity, high permeable bioclastic Cretaceous shelf sand (Åsgard sandstones) overlying a Silurian and/or Ordovician basement (as seen in 16/1-15). The Åsgard sandstones are draped over most of the northern, western, and south-western parts of the field, pinching out eastwards. Also, when the granitic basement is fractured and altered it has proven to exhibit producible reserves (e.g. long-term production test in 16/1-28 S, now known as Troldhaugen).

3 Modeling

In this section, we briefly describe the flow model and the approach for simulating seismic data. The latter section is divided in two main parts: the petro-elastic model and the seismic model.

3.1 Flow model

In this study, we have used the open-source reservoir simulator Flow [29], developed in the Open Porous Media (OPM) initiative. This simulator solves a black-oil (i.e., two hydrocarbon components) flow model using a fully implicit numerical scheme. The reservoir properties are defined on a hexahedron (corner point) grid and pressure-volume-temperature properties, as well as relative permeabilities and capillary pressures, are defined using tables. The boundaries are defined using no-flow Neumann conditions. Each well is modeled using multiple segments, and well equations are solved fully implicitly and coupled with the reservoir equations. Correlations between pressure and flow rates in well pipelines are modeled using tables. The non-linear system of equations is solved iteratively using a Newton-Raphson method. For each iteration step, a linearized system of equations is solved using a stabilized bi-conjugate gradient method with ILU(0) preconditioning (the generalized minimal residual method was also tested, but the bi-conjugate approach was superior for our reservoir model).

Two versions of the reservoir model for the Edvard Grieg field were used in this study. Both versions have the same configuration of wells. The 2018 model is developed using knowledge from data until 2018 and has 8,626,176 grid cells, of which 1,482,594 are active (in-active grid cells have no flow passing through them, and do not contribute to the numerical solution). The grid dimension in x-, y-, and z-direction is $128 \times 192 \times 351$. The other model was developed in 2020 and has slightly adjusted original hydrocarbon volumes in place. In addition, the model size is 12,254,400 grid
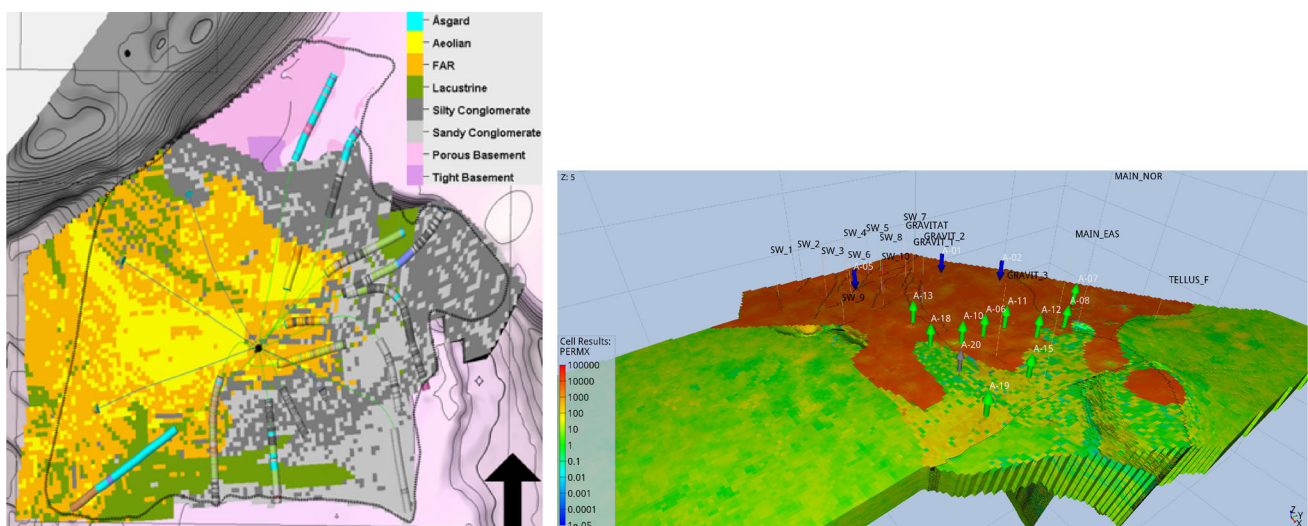
Fig. 1 Facies map (*left*) and permeability (*right*). The figures also show the location of wells and faults

cells, of which 1,559,040 are active. The grid dimension in x-, y-, and z-direction is $144 \times 230 \times 370$. The main difference between the two models is the incorporation of a new conceptual depositional model to reflect and simulate the dynamic behavior seen from the production and seismic data.

3.2 Simulation to seismic

The success of quantitative assimilation of seismic data in history matching depends on a good seismic forward modeling workflow that generates realistic seismic data based on the reservoir models. The workflow is referred to as "sim2seis" where the main objective is to simulate synthetic seismic data and attributes that are then compared with field seismic data to reduce the mismatch while updating various reservoir parameters [28]. The whole process can be divided into two parts: the petro-elastic model (PEM) and seismic modeling. A brief description of them is given below.

3.2.1 Petro-elastic model

A key part of the 4D workflow is the petro-elastic model (PEM) or rock physics model (RPM) for the different facies/rock types, which is needed to compute the elastic properties from the static and dynamic properties in the simulation model. It has not been the focus of this project to develop a new PEM for Edvard Grieg. Consequently, the project has relied on already existing models provided by the Operator, and neither the underlying PEM/RPM nor the uncertainties related to these have been assessed by this work.

In establishing the Edvard Grieg PEM the Operator has defined four main facies groups from the geological framework presented in Section 2:

- Sandstones; include aeolian, fluvial, reworked fluvial and aeolian, and bioclastic shelf sand.
- Alluvial fan conglomerates; consist of conglomerates with a sandy matrix and conglomerates with lower properties due to either: 1) matrix of low reservoir quality (silty), or 2) that they are dominated by large clasts and that the amount of effective matrix is limited.
- Basement; both weathered and porous basement (containing matrix properties) and hard and fractured basement. The latter with porosity only in fractures.
- Non-reservoir; predominantly lacustrine shales.

The Operator has supplied the project with appropriate dry rock elastic property-porosity relations (i.e. power laws for bulk and shear moduli, and density) per sandstone reservoir facies based on log data from exploration and appraisal wells. While the sandstones on Edvard Grieg in general follow well-established elastic property-porosity relations such as the

friable sand model [2], the conglomerates behave differently. It can be shown that the bulk modulus for conglomeratic facies on Edvard Grieg seems to increase (stiffen) faster with decreasing porosities compared with the shear modulus. It is believed that this could be linked to the nature of conglomeratic rocks, which can be seen as a "two-phased" medium with load-bearing clasts and in-between matrix. The clasts in the alluvial sand conglomerates are considered to be quite tight and not contributing to the net, while the matrix in the sandy matrix conglomerate shows medium to good reservoir properties [24]. Consequently, depending on the clast/matrix ratio, the effective porosity of the total rock can be quite low. To reflect this in the modeling scheme a different RPM strategy was required for the alluvial sands compared to the sandstones.

Avseth et al. [3] showed how the elastic properties of a low-to-intermediate-porosity sandstone could be described by combining the constant cement (CCT) and differential effective medium (DEM) theories. At the low porosity interval ($0 \leq \varphi \leq \varphi_{\mathrm{max,DEM}}$) they introduced pores of various shapes as inclusions in an effective mineral as the "host rock" using DEM. Rock Physics Technology (RPT, 3rd party consultancy company) on behalf of the Operator showed that this model could work as a proxy for modeling the effects of the presence of clasts in the conglomerates by treating the clasts as "spherical pores" in the effective sandy matrix as host in the same low porosity interval. Then the clasts would act as a reinforcement/stiffening of the rock framework, i.e. increasing the incompressibility, while their spheroid shape would mean that they do not increase the resistance against shear forces. The shear modulus would then be computed using Hashin-Shtrikman-Walpole lower bounds [31, 32] at intermediate and lower porosity ranges, which is also used to connect the low- and high porosity end member models for the bulk modulus. As the high-porosity end-member, RPT suggested using the Patchy cement model [1]. This variant of the [3] model is referred to as the Reinforced Kite model by RPT. For the non-reservoir facies groups, simple power laws and average values have been used to derive the p-wave and s-wave velocities and densities needed for seismic modeling. For simplicity, it is assumed that these facies groups have no or negligible 4D effects, and their elastic values will remain constant through time.

3.2.2 Seismic modeling

In this work, for seismic modeling, we have used the workflow developed by [16]. The idea is to model seismic data from a reservoir model or geo-model while honoring fundamental seismic propagation like tuning effects, and lateral continuity, as well as eliminating numerical grid effects. The modeling workflow has two main steps: mapping reservoir properties into a geophysical domain using a dual model con-

cept and then seismic modeling using the advanced Kirchhoff seismic modeling scheme.

The dual model concept recognizes the need for various models for various disciplines (like reservoir, geophysical, geological) to describe the same underground, but for different applications and further can be mapped from one domain to another [16]. Here, the mapping can be defined as shown in Eq. 1, where $\mathcal{G}$, $\mathcal{R}$ and $\mathcal{S}$ are geological, reservoir, and seismic models of the underground $u(\vec{r})$, respectively.

$$\mathcal{G}(u(\vec{r})) \Leftrightarrow \mathcal{R}(u(\vec{r})) \Leftrightarrow \mathcal{S}(u(\vec{r})) \Leftrightarrow \mathcal{G}(u(\vec{r})) \qquad (1)$$

The idea is to construct the mapping that is compatible with the geophysical model in parallel with the reservoir/flow model or the geo-model [17]. For example, reservoir/ flow models are parametric in nature, while seismic is usually modeled on a regular grid (such as a Cartesian grid). Therefore, mapping from one domain to another should honor these aspects.

First, we use the petro-elastic model to obtain seismic properties (such as V_p, V_s, density) in reservoir cells. These uniform cell properties (defined in the reservoir sample grid) are then mapped into a geophysical model/ domain (Cartesian grid or regular grid). The mapping is done by projecting the reservoir properties vertically to the cell interfaces and mapping the structural grid to seismic bin positions as follows [16]:

- Grid all cell top and base boundaries from reservoir structural model corner points to reflective surfaces based on seismic bin positions
- Project reservoir sample grid properties to reflective surfaces and interpolate reflectivity based on reflective surface sample points
- Interpolate velocity based on reservoir sample grids within layers

Further, we follow some additional steps to fill and fix the geophysical model that is to be used for seismic modeling. For example, in the current approach, the undefined cells are filled with average properties of the individual layers. The zero-cell thickness grid properties are filled with linear interpolation vertically. In addition, an overburden model is used to obtain a realistic seismic response from the top of the reservoir. Here, the overburden model (static elastic model) is constructed by interpolating well-log information that conforms with the structural model of the reservoir grid.

Once the reservoir properties are mapped into the regular grid, the seismic modeling scheme is used to generate a seismic response. As the reservoir model has varying scales from + 100 m to 1 mm (mainly at pinch-outs area), both simple convolution algorithms model and advanced finite difference modeling are not appropriate for this kind of scenario. This

may lead to numerical artifacts in the modeled seismic. Finer gridding can improve the results but comes with a significant computational cost. In addition to the lack of vertical resolution from imaging the reflected wave field, the simple convolution algorithms model is not capable of modeling the inevitable lack of lateral resolution. Thus the horizontal resolution is often over-predicted. Therefore, to address these issues, an approximation of the combined Kirchhoff modeling and imaging operator known as the point spread function is implemented with acceptable runtime. More details of the modeling can be obtained in [11, 16, 17].

Realistic seismic noise modeling is usually not carried out in detail. Gaussian or vertically filtered Gaussian noise is often generated, where scaling is done in some ad hoc way. However, high-frequency noise in any spatial direction is usually removed in data processing and is in that respect a poor approximation of seismic noise. A more realistic noise estimate takes into account that we have tried to image our data and eliminate noise in the best possible way. The noise that is remaining, is the noise that is indistinguishable from data. To model realistic seismic noise an approach that generates noise that resembles data as accurately as possible is adopted.

4 Methodology

Here we present the workflow for updating model parameters. We start with a description of how the prior models are generated, followed by the main methodology for data assimilation including the Bayesian inversion technique, localization, and data compression.

4.1 Prior model

The prior ensemble is built from perturbations of selected parameters. We consider three-dimensional field parameters defined on all grid cells, two-dimensional surface parameters, and scalar parameters. We use three different techniques for generating perturbations of the parameters. The direct way consists of using normal (Gaussian) distributions to generate (possibly correlated) realizations of a parameter type. This approach is used for, e.g., porosity and permeability. The realizations are generated using a Gaussian variogram, and in this case, it is possible to directly generate correlated Gaussian random fields. The methodology for doing this is to our knowledge not yet published, but the algorithm can be found in [26, `gaussian_sim.py`]. In this study, reservoir properties are implicitly conditioned on well-log data by using a reference model (provided by the operators) as the mean for the distributions. No additional conditioning is applied, in order to account for the uncertainty related to upscaling of log data. If a normal distribution is used, it is nec-

essary to truncate the updated parameters if they fall outside predefined physical bounds. Other parameters are better characterized using log-normal distributions, e.g., permeability. In this case, a normal distribution with mean $\bar{\mu}$ and standard deviation σ is used to populate the ensemble, but an exponential transformation is used before the parameters are exported to the simulator. The transformed distribution for the parameters will then have a log-normal distribution with mean $\exp(\bar{\mu} + \sigma^2/2)$. In this case, the parameters will always be positive, but truncation might still be necessary to restrict the range of the values. We use a hard cut-off in our study. Some parameters (i.e., relative permeabilities and fault multipliers) are best represented as uniformly distributed on a closed interval. In this case, we start with a standard normal distribution Z (i.e., zero mean and standard deviation equal to 1), and transform the parameters using the cumulative distribution function (cdf) before the parameters are exported to the simulator. In addition, scaling is applied to obtain the required upper and lower bounds. This transformation is summarized as $Y = \text{cdf}(Z) \times (b - a) + a$, where a and b are the lower and upper bounds, respectively. In this case, no truncation is necessary as Y will always be within $[a, b]$.

4.2 Model calibration

Ensemble-based data assimilation is performed to automatically calibrate the model. The methodology is based on a Bayesian description of the problem, where we update the poorly known prior state of the system by calibrating – or conditioning – to the measured data. Assuming that we have a Gaussian prior model and Gaussian measurement error, Bayes' theorem gives the following equation for the posterior distribution of the calibrated model

$$p\left(\vec{m}|\vec{d}_0\right) \approx e^{-\frac{1}{2}\left[\left(\vec{g}(\vec{m})-\vec{d}_0\right)^T C_d^{-1}\left(\vec{g}(\vec{m})-\vec{d}_0\right)+\left(\vec{m}-\vec{m}_{prior}\right)^T C_m^{-1}\left(\vec{m}-\vec{m}_{prior}\right)\right]}. \tag{2}$$

Here, $\vec{m} \in \mathbb{R}^{N_m}$ is the vector of model parameters; $\vec{d}_0 \in \mathbb{R}^{N_d}$ is the vector of measurements; $\vec{m}_{prior}$ is the prior mean vector for the parameters; $\vec{g} : \mathbb{R}^{N_m} \to \mathbb{R}^{N_d}$ is the simulator mapping the parameters into the data space which in this study consists of the fluid flow simulator coupled with the sim2seis; $C_m \in \mathbb{R}^{N_m \times N_m}$ is the parameter covariance matrix; and $C_d \in \mathbb{R}^{N_d \times N_d}$ is the measurement covariance matrix. In the EnRML method, we seek to generate samples from Eq. 2 by first generating an unconditional (rough) sample from the prior and measurement distributions, and then correcting this model by minimizing the exponent in Eq. 2.

The EnRML method does not require any given minimization method. However, the Levenberg-Marquardt method has been shown to work very well for subsurface flow problems, see, e.g., [7, 19]. Here, we calibrate the model using EnRML with the approximate formulation of the Levenberg-Marquardt method, as introduced in [6]. Unconditional samples of the prior and measurements are drawn from the respective distributions. The lth iteration of the minimization for sample j is given by

$$\delta\vec{m}_{l+1,j} = -\left((1+\lambda_l)\,C_m^{-1} + G_l^T\,C_d^{-1}\,G_l\right)^{-1}$$
$$\times \left[C_m^{-1}\left(\vec{m}_{l,j} - \vec{m}_j^{\text{prior}}\right) + G_l^T\,C_d^{-1}\left(\vec{g}\left(\vec{m}_{l,j}\right) + \vec{\epsilon}_j - \vec{d}_0\right)\right], j = 1 \ldots N_e, \tag{3}$$

where G_l is the sensitivity of measurements to the model state, where one element is given as $G_{i,j} = \partial g_i/\partial m_j$, and λ_l is the Levenberg-Marquardt inflation factor for the Hessian. The ensemble size is denoted N_e, and $\vec{\epsilon}_j$ is a realization of the measurement noise drawn from a Gaussian distribution with zero mean and covariance C_d. To obtain the approximate form, Eq. 3 is simplified by neglecting the terms containing the mismatch of the model parameters, and the equation is rewritten by applying the Sherman-Woodbury-Morrison matrix inversion formulas [13]. This gives

$$\delta\vec{m}_{l+1,j} = -C_m G_l^T\left[(1+\lambda_l)\,C_d + G_l C_m G_l^T\right]^{-1}\left(\vec{g}\left(\vec{m}_{l,j}\right) + \vec{\epsilon}_j - \vec{d}_0\right). \tag{4}$$

Extracting the sensitivity of measurements to the model state is notoriously difficult for reservoir simulators. To avoid this EnRML approximates G_l from the ensemble, see, e.g., [14] as

$$G_l = \Sigma_d^{1/2}\,\Delta D_l\,(\Delta M_l)^{-1}. \tag{5}$$

Here, ΔM_l is the centered and scaled ensemble of model properties at the $(l)^{th}$ iteration,

$$\Delta M_l = \left[\vec{m}_{(l,1)}, \ldots, \vec{m}_{(l,N_e)}\right]\left(I_{N_e} - \frac{1}{N_e}\vec{1}\vec{1}^T\right)/\sqrt{N_e-1}, \tag{6}$$

where $[\vec{m}_{(l,1)}, \ldots, \vec{m}_{(l,N_e)}]$ is the N_e members of the ensemble of model properties, I_{N_e} is the N_e-by-N_e identity matrix, and $\vec{1} \in \mathbb{R}^{N_e}$ is the column vector of ones. Similarly, ΔD_l is the centered and scaled ensemble of predicted measurements at the $(l)^{th}$ iteration

$$\Delta D_l = \left[\vec{g}(\vec{m}_{(l,1)}), \ldots, \vec{g}(\vec{m}_{(l,N_e)})\right]\left(I_{N_e} - \frac{1}{N_e}\vec{1}\vec{1}^T\right)/\sqrt{N_e-1}, \tag{7}$$

where $\left[\vec{g}(\vec{m}_{(l,1)}), \ldots, \vec{g}(\vec{m}_{(l,N_e)})\right]$ is the ensemble of predicted measurement, i.e. the result of applying the forward simulator, $\vec{g}(.)$, to the ensemble of model properties at the $(l)^{th}$ iteration. Finally, $\Sigma_d^{1/2} \in \mathbb{R}^{N_d, N_d}$ is a scaling matrix to approximately normalize the data.

To make the method numerically stable, a truncated Singular Value Decomposition (SVD) of ΔD_l is performed

$$\Delta D_l = U_p\,S_p\,V_p^T, \tag{8}$$

where the subscript p denotes the truncation level. That is, we sort the singular values in descending order and retain the first p values. The value of p is selected such that the sum of the first p values corresponds to 98% of the sum of all singular values. The remaining singular values, with their corresponding singular vectors, are discarded. Inserting Eqs. 5, 6, 7, 8 into Eq. 4 and simplifying, we obtain

$$\delta \vec{m}_{l+1,j} = -\Delta M_l \, V_p \, S_p \left[(1 + \lambda_l) \, I_p + S_p^2 \right]^{-1} U_p^T \, \Sigma_d^{-1/2} \left(\vec{g} \left(\vec{m}_{l,j} \right) + \vec{\epsilon}_j - \vec{d}_0 \right), \tag{9}$$

where we have also used the ensemble to approximate $C_m \approx \Delta M_l \Delta M_l^T$.

The iteration described by Eq. 9 is repeated until the stopping criterion is reached. In the numerical study, we stop the iteration when the relative improvement in data misfit is below a predefined threshold. In addition, to improve convergence, we adapt λ_l for each iteration. For more information about convergence criteria and updating rules for λ_l, we refer to [18, 21].

4.3 Localization

The ensemble-based data assimilation method calculates the updates based on Monte-Carlo estimates of covariance and cross-covariance. Since we have limited computational resources, we can only afford to run a relatively modest ensemble of subsurface flow models. Hence, there is a substantial sampling error associated with the Monte-Carlo estimates. It is well known that localization can be used to mitigate this sampling error.

There are numerous localization schemes available in the literature. Typically, some sort of distance-based tapering has been applied where updates are dampened as a function of the distance between the parameter and data. Updates beyond a user-defined critical distance are set to zero. Unfortunately, these schemes have some drawbacks if data or parameters don't have a spatial position, see, e.g., [23]. An alternative localization method, more suitable for large models with large data, is based on the value of the estimated correlation between the parameters and data. Updates pertaining to correlation below a user-defined threshold are dampened – or set to zero. This localization scheme is denoted as *correlation-based adaptive localization* [20].

The update defined in Eq. 9 can be rewritten in matrix form as

$$\delta M_{l+1} = -\Delta M_l R_l, \tag{10}$$

where $R_l \in \mathbb{R}^{N_e \times N_e}$ is a matrix where the columns hold the projection of the ensemble of residuals. In the same spirit as [20], we define the localized update as

$$\delta M_{l+1} = - \left(C \circ \Delta M_l \right) R_l, \tag{11}$$

where $C \in \mathbb{R}^{N_m \times N_e}$ is the matrix of tapering coefficients and $\circ$ defines the Schur product. The element of C is given as

$$c_{i,k} = \mathcal{I} \left(\text{abs} \left(\rho_{i,k} \right) > \Theta_{i,k} \right), \tag{12}$$

where $\mathcal{I} \left(\cdot \right)$ is the indicator function, $\rho_{i,k}$ is the Monte-Carlo estimate of correlation between parameter i and projected data k, and $\Theta_{i,k}$ is the threshold value for the localization.

The indicator function is one if the condition is fulfilled and zero if the condition is not fulfilled. Hence, it acts as a cut-off where only updates with a correlation above the threshold are kept. Alternatively, one could apply a different taper function. Luo and Bhakta [20] applied the Caspari-Cohn function as a continuous taper, and we have also tested various forms of the Sigmoid function. Figure 2 illustrates the difference between these approaches.

The Monte-Carlo estimate of correlation is affected by sampling noise. Ideally, one would therefore like to set the threshold value equal to the noise level. To approximately achieve this, the threshold value for the localization can be calculated following the efficient procedure given by [20]. The procedure randomly shuffles the columns of Eq. 6 and calculates the correlation between the shuffled parameters and the projected data (denoted ϵ_ρ). Since the parameters are sampled as independent and identically distributed random variables, the shuffling ensures that the correlation is theoretically zero, and ϵ_ρ can therefore be considered as an estimate of the noise. Further, the standard deviation for this noise can be approximated using the median absolute deviation (MAD) estimator

$$\sigma = \frac{\text{median} \left(\text{abs} \left(\epsilon_\rho \right) \right)}{0.6475}. \tag{13}$$
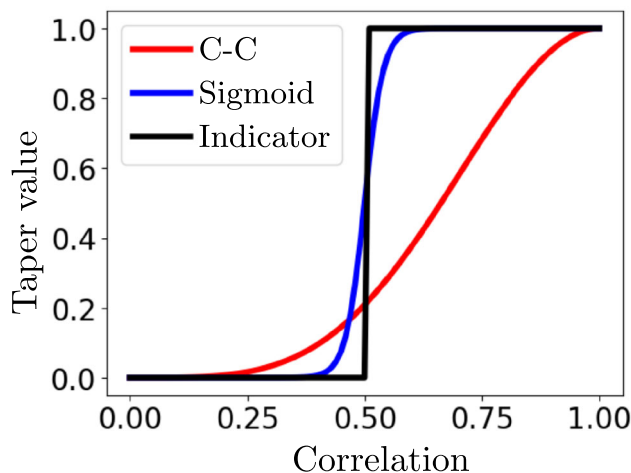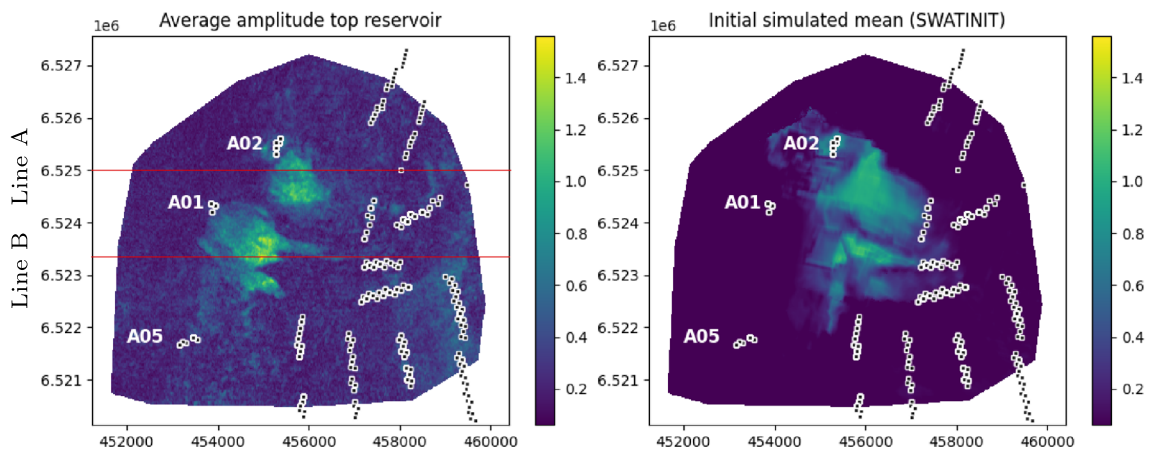

Fig. 2 Taper value as a function of estimated correlation for different taper functions. For all functions, $\Theta = 0.5$. Caspari-Cohn is abbreviated C-C

Fig. 3 Map from averaging absolute amplitudes in a window from 50 ms above to 50 ms below the reservoir top. The figure shows the map based on the difference between the 2016 base survey and the 2018 monitor survey (*left*) and the initial simulated mean of the amplitude maps (*right*). The results on the right figure are based on using simulated SWATINIT for initialization. The axes show the UTM coordinates and the colorbar shows the signal strength. The cells that are completed by the wells are shown as white circles. The injectors are on the reservoir's west side and are labeled A-02, A-01, and A-05. The producers are also shown, but not labeled. The horizontal red lines (labeled Line A and Line B) indicate the slices that are discussed in this section

The threshold is then given as $\Theta = \tau \cdot \sigma$, where τ is a user-defined scaling. A unique taper function is calculated for each of the parameter types.

4.4 Data compression

An important part of the methodology is the compression of data for the reduction of required computer memory. We follow [19, 22], but the techniques introduced there are modified to further include information in the simulated data. We focus on minimal compression loss in areas where the data show significant seismic information, in addition to the areas where the models show false information (i.e., areas where the modeled seismic signal is not seen in the actual data). The updated procedure can be summarized as follows: Discrete wavelet coefficients $\vec{c}_j$ are computed for the inverted seismic attributes and the simulated attributes. Denoting the actual data as $\vec{d}_0$, and simulated data as $\vec{d}_j$, $j = 1 \ldots N_e$, this can be written $\vec{c}_j = \text{DWT}(\vec{d}_j)$. Further, a median absolute

deviation estimator can be used to compute the standard deviation for the noise associated with the wavelet coefficients. We emphasize that these quantities are from a perspective of image denoising, and do not necessarily represent all sources of error in the seismic data. The estimated noise for the coefficients can however be correlated in space and are suitable for computing thresholds T_j separating leading wavelet coefficients from coefficients of minor importance. Denoting the index-set of leading coefficients by I_j, our compressed data (either measured or simulated) is defined as $\{c_i\}$, $i \in I$, where $I = \cup I_j$. In our study below we apply data compression for the large impedance cubes. No compression is used when assimilating amplitude maps.
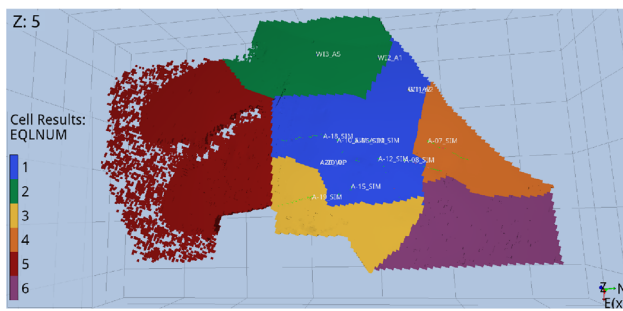
5 Results

The results are divided into three main categories: preliminary results showing investigations of deficiencies in
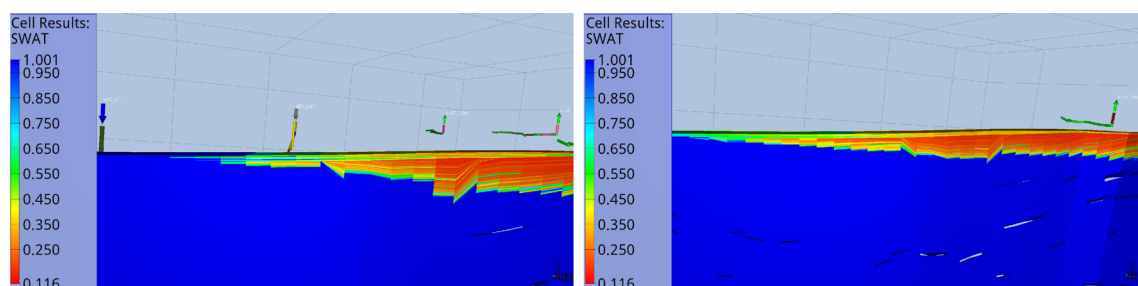
Fig. 4 Initial water saturation using cell-based values (SWATINIT) (*left*) and using oil-water contacts (OWC) (*right*) for Line B. The left picture shows wells that are open both initially and later in the production. The right figure only shows the well that is open initially (producer A-11)

Fig. 5 The six equilibrium regions in the Edvard Grieg field

the prior model description and suggestions for improvements, results using two-dimensional amplitude maps, and results using three-dimensional impedance cubes. The section focusing on amplitude maps is the most comprehensive and includes model checking, data match, estimated parameters, and model validation.

5.1 Preliminary studies

A preliminary study based on a fraction of the data was carried out using the 2018 model. Through this study we gained valuable knowledge about the shortcomings and important aspects of the reservoir and the model, enabling us to include the governing parameters in the data assimilation. We considered the seismic amplitude map based on the difference between the 2016 base survey and the 2018 monitor survey. The amplitude map is calculated from full stack amplitude versus offset (AVO) data, by averaging absolute amplitudes in a window from 50 ms above to 50 ms below the reservoir top. The field data are time-shift corrected. We used a pre-generated cell-based property for the initial water saturation (SWATINIT) for the Edvard Grieg field. Figure 3 shows the field data and the mean of simulated amplitude maps. From the field data, we identify a clear signal close to the upper water injector (A-02), and a clear signal close to the middle water injector (A-01). These signals are coming from injected water and the waterfront moving from west to east. However, the simulated signals are too strong, and the water is mov-

ing faster than the data indicates. Investigations of the initial water saturation revealed a discrepancy between the provided cell-based values and the oil-water contact generated based on well logs. Figure 4 shows a cross-section in the west-east direction, going through the southern field amplitude signal (see Line B on Fig. 3). The left plot shows a simulation using SWATINIT and the right plot shows a simulation where initial water saturations are generated using the oil-water contacts (OWC). We clearly see that the oil zone pinches out earlier on the left picture compared to the right picture. The consequence of an early pinch-out is that there will be no water replacing oil in this part of the reservoir, and the waterfront appears to move faster. There are six equilibrium regions in the reservoir model, each having a different oil-water contact. The six regions are based on information in the seismic data and are shown in Fig. 5. The zone between the injectors and the producers is mainly covered by equilibrium regions 1 and 2.

The size of the simulated northern amplitude signal (near A-02) is too large compared to the field data. We found that one reason for this is a substantial flow from the water zone (aquifer) into the oil zone. This is illustrated in Fig. 6. The figure shows a cross-section in the west-east direction, going through the northern field amplitude signal (see Line A on Fig. 3). Strong influence from the aquifer is an indication of high vertical permeability, and reduction of the vertical permeability is a plausible remedy for correcting the spurious simulated amplitude signal. Figure 7 shows the current vertical permeability for Line A.

The above considerations motivated us to include uncertainty for the oil-water contact (OWC) and a vertical permeability multiplier (MULTZ) when generating the initial ensemble. The benefit of doing so is illustrated in Fig. 8, where the bottom plots show an average over an ensemble of simulated amplitude maps. The northern signal is weakened in the vicinity of injector A-02 and around producer A-11 (marked on the top left plot) in the east. The signal is also strengthened approximately where the data show a change. The differences are more prominent in the south. The western part of the signal is enhanced and the eastern part of the
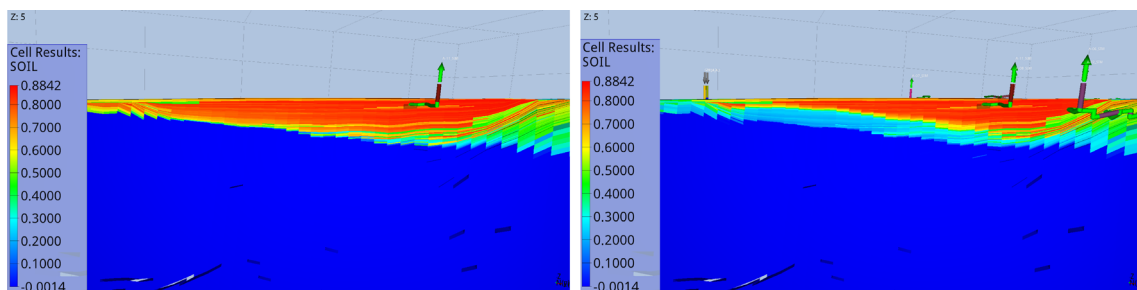
**Fig. 6** Initial (*left*) and final (*right*) oil saturation for Line A
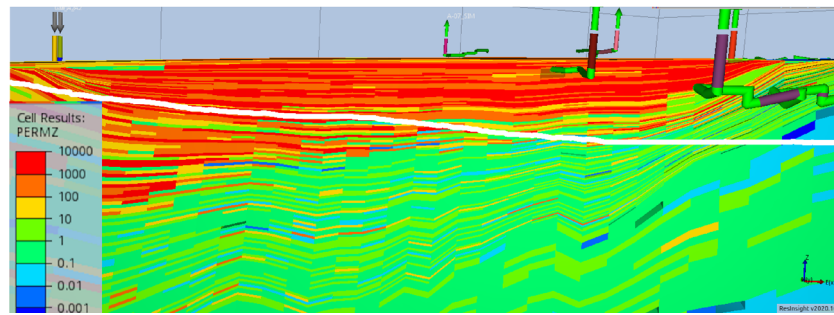
Fig. 7 Vertical permeability (PERMZ) for Line A. The white line indicates the initial OWC (see also Fig. 6)

signal is weakened. The improvements stem from the use of oil-water contacts instead of pre-generated water saturations, and from introducing uncertainty for the vertical permeability. Note that for this ensemble we selected a distribution with a mean value less than unity (1) for MULTZ.

5.1.1 Value of seismic data

The 2018 model was run both with and without using the seismic data. Although the case using only well data had slightly different prior distributions, the cases illustrate the
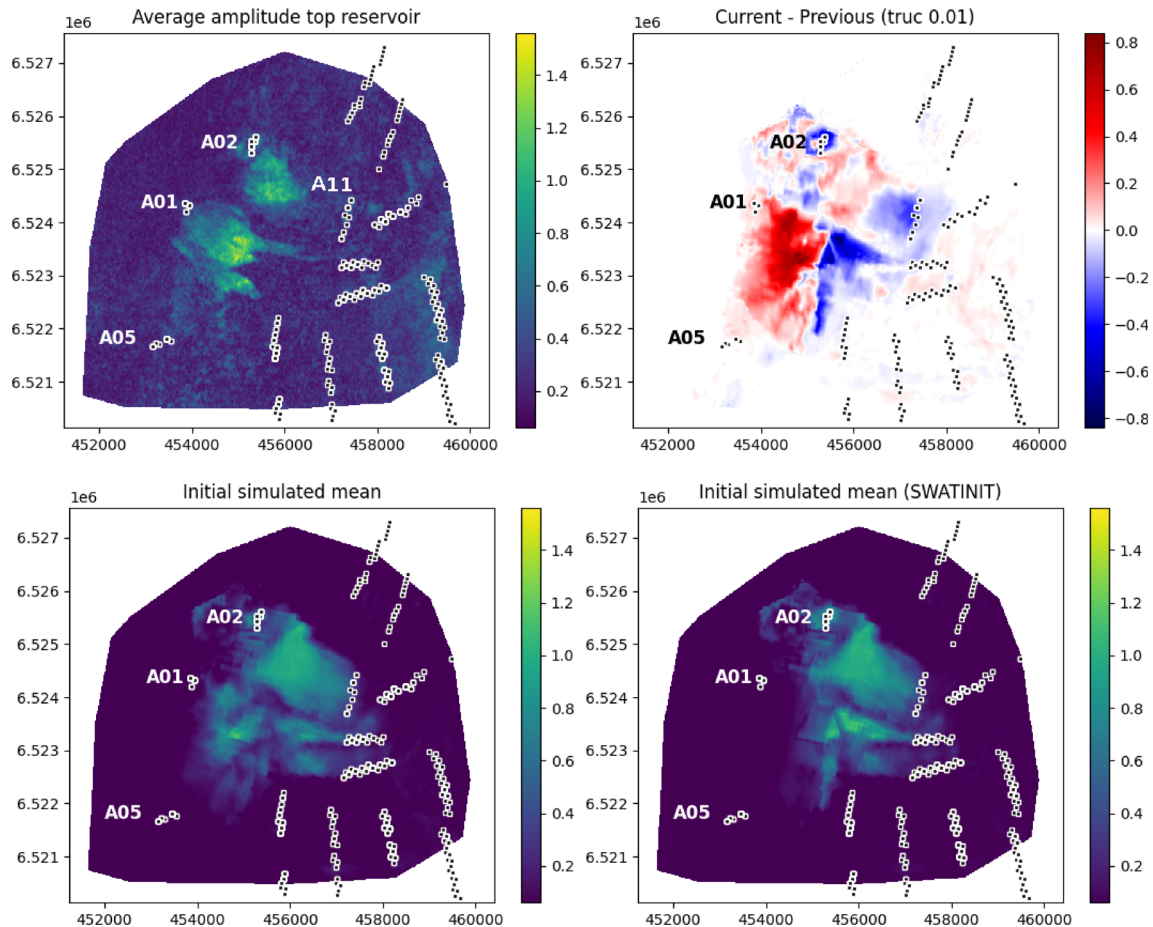
Fig. 8 Map from averaging absolute amplitudes in a window from 50 ms above to 50 ms below the reservoir top. Amplitude map based on field data (*top left*), simulated amplitude mean maps after including MULTZ and OWC (*bottom left*), mean of the simulated amplitude maps when using initial water saturation (*bottom right*), and the difference between the simulated results (*top right*). The top right plot only shows differences larger than 0.01
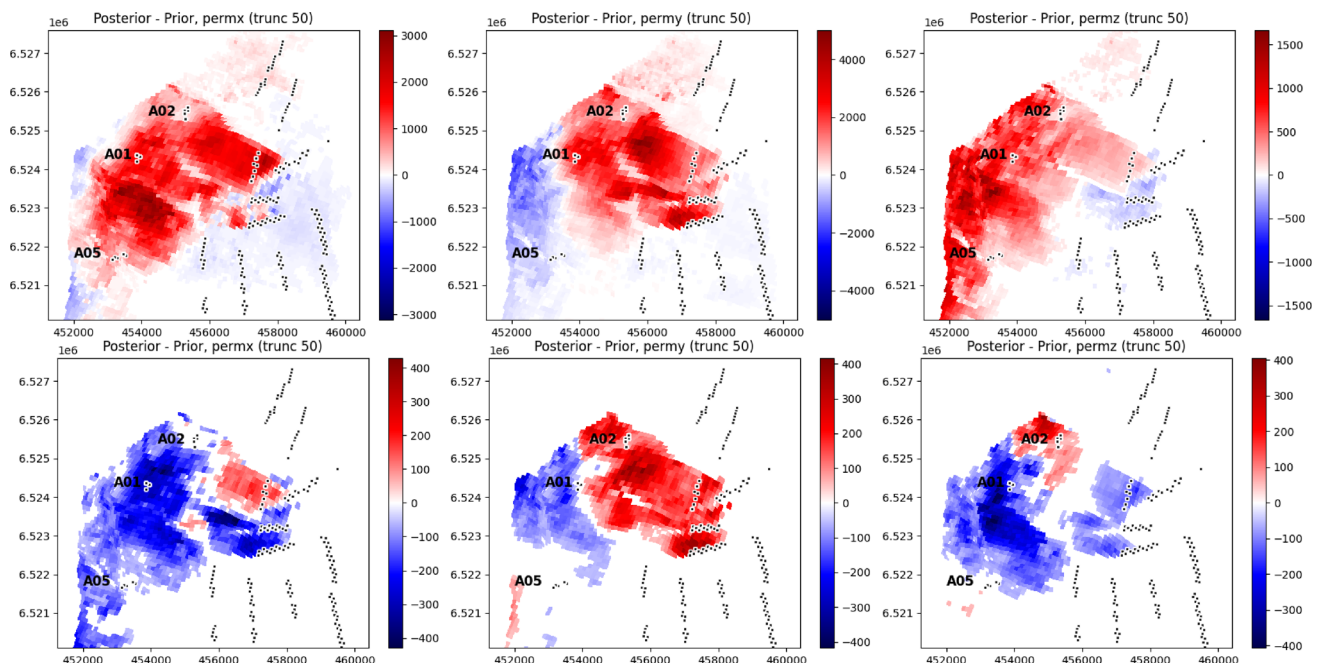
Fig. 9 Difference between posterior and prior permeability estimate [mD] in x-, y-, and z-direction. Values below 50 mD are not shown on the plots. *Top*: Results based on well data only. *Bottom*: Results based on both well data and seismic data
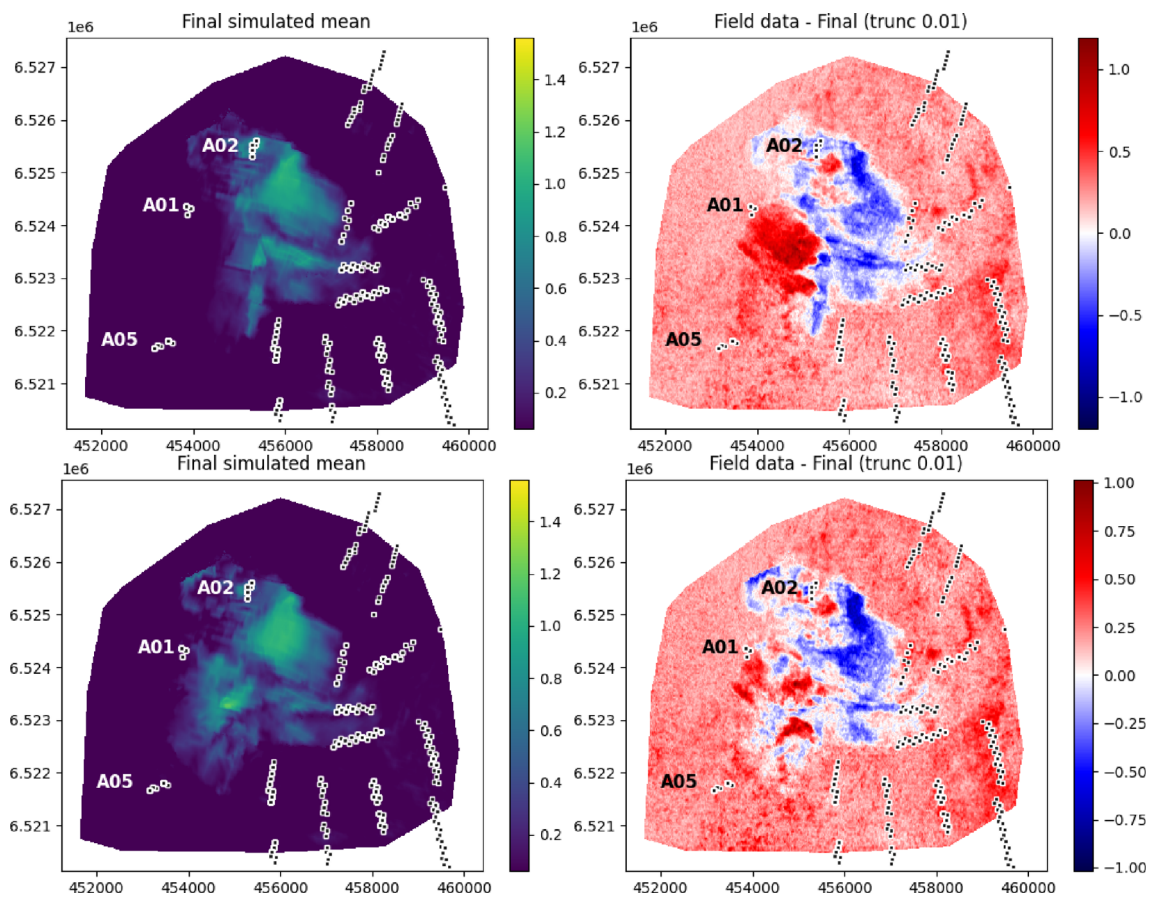
Fig. 10 Simulated seismic data based on posterior parameters (*left*), and the difference between the simulated seismic and the field data (*right*). Values below 0.01 are not shown on the plots. *Top*: Results based on well data only. *Bottom*: Results based on both well data and seismic data

Table 1 Standard deviations for measurement errors

Data type	std (σ)	Unit
Oil rates	200	Sm^3/day
Water rates	20	Sm^3/day
Gas rates	20000	Sm^3/day
BHP	10	Bar
RFT	2	Bar

value of including seismic data. Figure 9 shows the difference between posterior and prior permeability in all directions with and without seismic data. Especially in the x- and z-directions, there is a clear shift from positive to negative change in the estimated permeability. When seismic data are assimilated, it is important to precisely model the waterfront movement, and the permeability in the x-direction is updated for this purpose. Also, as discussed above, the permeability in z-direction influences the vertical water movement, which is also crucial for matching the seismic data.

In Fig. 10 we show the simulated seismic data without (top) and with (bottom) assimilation of seismic data. The average seismic data mismatch (see Eq. 15) without assimilation of seismic data is 5.99 and the average seismic data mismatch with assimilation of seismic data is 1.76.

5.2 Assimilating amplitude maps

We continued our investigations using the 2020 model for the Edvard Grieg field. This model allowed us to utilize two seismic monitor surveys, in addition to the base survey. We generate two datasets from the seismic surveys. The first dataset is the difference between the 2018 monitor and the 2016 base survey, and the second dataset is the difference between the 2020 monitor and the 2018 survey. The production data were collected monthly from all wells in the period from November 2015 until August 2020. We also

used the repeat formation tester (RFT) data and the bottom hole pressures (BHP) from the wells. The properties for data uncertainty and the prior model are summarized in Tables 1 and 2. In this study, data uncertainty is automatically inflated if a field value is not covered by the prior prediction. The inflation is proportional to the shortest distance between the measured value and the ensemble of predicted data. We did not include correlated errors for the well data. A detailed discussion of the impact of correlated errors is found in [10]. The initial damping factor (Section 4.2) is $\lambda_0 = 5000$, and adaptive localization (Section 4.3) is used with a truncation scaling $\tau = 1.5$. The convergence criterion (Section 4.2) is 0.01, and a scaling factor of 0.5 is used to down-weight the seismic data compared to production data. See [19] for more information regarding the scaling of different data types.

Based on the preliminary studies we decided to continue initializing the model using oil-water contacts and to include oil-water contacts and multipliers of the vertical permeability in the prior ensemble. In addition, we included the top surface of the reservoir as an uncertain parameter. More specifically, we defined the top surface as the interface between the Åsgård sand and the Shetland chalk. In this study, we did not modify the top surface between the conglomerate and the chalk. The sand layer is highly permeable, and thereby a very good conductor of both fluids and pressure. The perturbations we generate for the reservoir top are conditioned on the depth at the well locations, as we assume that the depths at these positions are accurately measured and we do not want the wells to appear outside the high-permeable sand layers. We decided to exclude uncertainty for the net-to-gross, and instead, allow the uncertain porosity to determine the pore volume in the reservoir. Finally, since the bottom hole pressures are included as data, we add well production indices (WPI) as uncertain parameters. This is crucial, as the flowing well pressures depend on local reservoir properties modeled using the production indices. The specification of the initial ensemble is summarized in Table 2.

Table 2 Mean, standard deviation, minimum, and maximum for the prior ensemble

Parameter type	mean (μ)	std (σ)	min	max
Top	μ_{ref}	2		
Porosity	μ_{ref}	0.0625	0	1
Log-permeability (x, y, z)	$\log(\mu_{\text{ref}}) - \sigma^2/2$	0.2	-5	10
Multz (cfd)	0	1	0	2
OWC	μ_{ref}	2		
Log-WPI	$0 - \sigma^2/2$	1		
Kr (w,o,g) (cfd)	0	1	0.75	1.25
Multpv (cfd)	0	1	1	3
Multflt (cfd)	0	1	0	1.2

Here μ_{ref} indicates the reference model (provided by the operator). For spatially distributed parameters, a variogram range of 40 gridblocks (in all directions) is used. See also Section 4.1
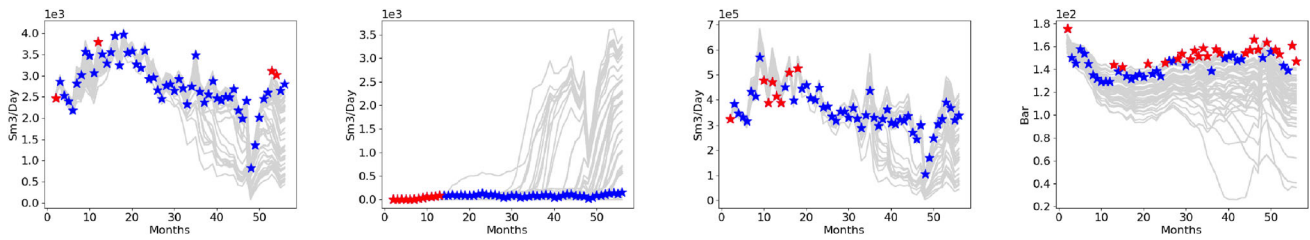
Fig. 11 Coverage for well A-10. The figure shows (from left to right): the oil production rate, water production rate, gas production rate, and bottom hole pressure. A blue asterisk indicates that the data point is covered, and the contrary for red

5.2.1 Model check

Before starting a data assimilation job, it is natural to investigate the plausibility of the generated prior models. In particular, it is necessary to investigate the coverage of the simulated data, with respect to the field measurements. In this work, we define coverage by how well the ensemble represents the domain of interest. I.e., if field data is included in the geometric envelope defined by the ensemble, the data is said to be covered by the ensemble. This task is rather simple for time-series production data, and in our workflow, we plot this coverage before starting the assimilation. This is illustrated for well A-10 in Fig. 11. The data are covered with a few exceptions, but the data that fall outside are close to the ensemble. In future versions of the coverage measure, we want to also account for the measurement uncertainty.

We have also developed a novel tool for visualizing the coverage of seismic amplitude maps, that is efficient for comparing a large number of seismic data with the ensemble. The methodology utilizes an importance attribute which identifies important data that are above the noise threshold. Coverage and importance are used to visualize the spatial area where the ensemble span covers the data and the area where a significant discrepancy exists. The methodology for computing the coverage plots is thoroughly described in [17]. Figure 12 (top) illustrates this for the two seismic datasets. The data are mostly covered but with some exceptions for the first dataset. The coverage plots are highly effective for locating areas where the simulated ensemble is not properly modeling the data, but they do not show how far data are from the ensemble span. To accommodate this, we also have the possibility to plot coverage for slices through the reservoir,
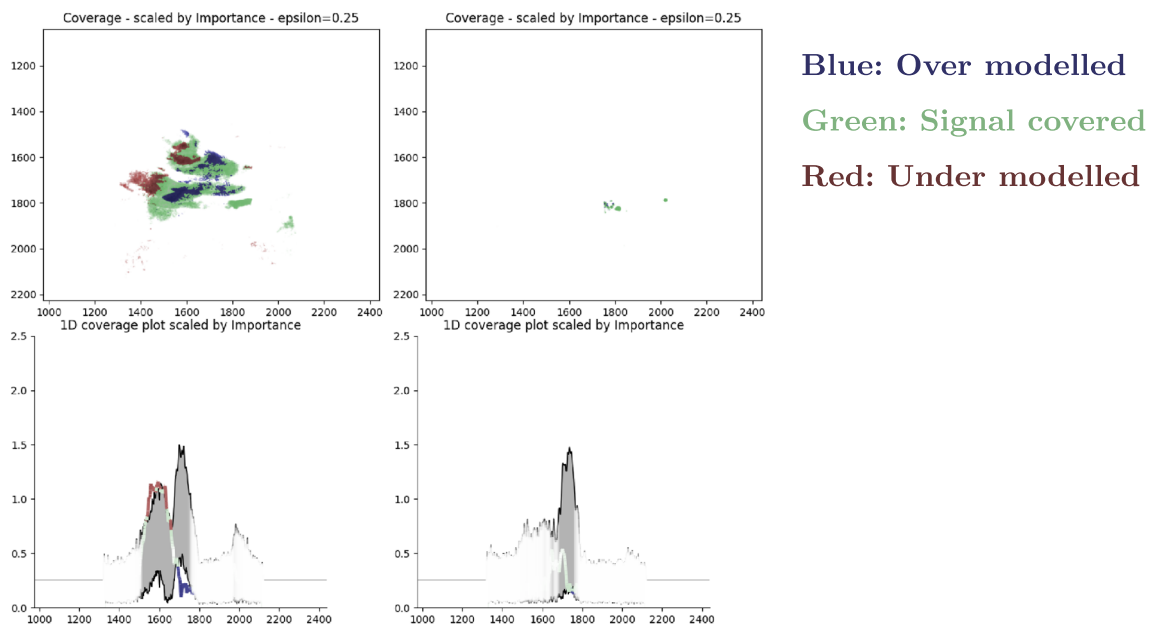
Fig. 12 *Top*: Coverage maps for first (*left*) and second (*right*) seismic amplitude dataset. The x- and y-axes show seismic crosslines and inlines, respectively. *Bottom*: 1D coverage plots for first (*left*) and second (*right*) seismic dataset at inline 1600. The x-axis shows the crosslines.

Green color indicates coverage, red is real amplitude not covered, blue is modeled amplitude not seen, and white is unimportant areas. Important areas require that both the ensemble and the field data are different from the noise floor

in either the x- or y-direction. Figure 12 (bottom) shows the coverage through inline 1600. From this figure, it is clear that all seismic field data along this inline are close to the ensemble (shown in grey).

A drawback with the coverage measure used for the time-series data above is that it is difficult to reveal inconsistencies in correlations between measurements since the data uncertainty is not taken into account. The Mahalanobis distance is therefore a better way to evaluate the credibility of the prior ensemble [27]. The Mahalanobis distance is used to measure the distance between a point and a distribution f, and is written:

$$D_M^2(d^o, f) = (d^o - \mu)C_p^{-1}(d^o - \mu), \tag{14}$$

where μ and C_p are the mean and covariance for the distribution f. In our application, the probability distribution is represented by the ensemble of perturbed simulated observations, and μ and C_p are sample estimates. If the measure is applied for a single observation (level 1) it will represent an improved coverage merit that takes measurement uncertainty into account. When applied to pairs of observations (level 2) it is an effective measure that also takes correlations between the data into account for identifying inconsistencies. The squared Mahalanobis distance can be compared with a chi-square distribution that represents a theoretical value for the measure. For a single observation, the theoretical number using a p-value equal to 0.01 is 6.6, and for pairs of observations, the corresponding theoretical value is 9.2 [27]. In our workflow, we compute the squared Mahalanobis distance for data in two different ways. In the first way, we compute the measure for each point in time. In the second way, we lump time-series data (or spatially distributed RFT data) together and project the ensemble onto the space spanned by the most dominant singular vector. The latter approach limits the amount of information since we only get one number for each data type. In Table 3 we display the top five score values using the second approach.

It is clear from the table that the pressure is particularly difficult to model using the prior ensemble. Well A-07 is the most problematic as it has the highest level 1 score, and it has the highest level 2 score when paired with the water pro-

duction in well A-20. Also, the RFT pressure at well A-18 is represented in the table, paired with bottom hole pressures from wells A-11 and A-07. Although the numbers slightly exceed the theoretical values we decided to continue working with this ensemble and use it for data assimilation. A visualization of the level 2 results is shown in Fig. 13. As we see, the field measurements are in the periphery of the ensemble cloud.

It is of interest to know which measurements are most influential on the parameter updates, and which parameters are most sensitive to the data. As part of our quality assurance workflow, we compute the Kalman gain (see Eq. 4) corresponding to each data-type, and rank the most influential data and the parameters they impact. In this study, the largest updates are seen for the reservoir depth parameter, and it is induced by the production data. More specifically, the pressure in wells A-01 and A-12 has the highest impact on the reservoir depth, but also the production rates are ranked high on the impact they have on the reservoir top. We have implemented the possibility of exporting the Kalman gain (as .grdecl files) for the different data types so that they can be inspected in a visualization tool such as ResInsight [4]. Figure 14 shows the change of the top depth (see Table 2) for the reservoir based on data from wells A-01 and A-12. A higher value means higher depth (i.e., pushing the top reservoir deeper), which is equivalent to a thinner oil column. From the sum of the two contributions (right plot), we see that the general trend is to lower the oil column in the region between the injectors and producers.

Figure 15 (left) shows part of the grid with the highest change in porosity [m^3/m^3] (small values are filtered out) from seismic data. The change is mostly positive (i.e., increased porosity), especially for the top layers between injector A-01 and the producers. The colorbar on the figure applies to all plots. The values are relatively small since this is a contribution from single datatypes at a single iteration step. The accumulated contributions from all datatypes and all iterations lead to the updated porosity that is discussed later (Section 5.2.3). For comparison, we also calculated the Kalman gain for oil production at well A-11 on porosity (right plot). Also here we see an increase of porosity at the top layers between well A-01 and the producers. There are some

Table 3 The level 1 and level 2 Mahalanobis measure

Data type	Level 1 D_M^2	Data types	Level 2 D_M^2
BHP A-07	11.9	WPR A-20, BHP A-07	10.8
BHP A-08	11.2	BHP A-11, BHP A-12	10.4
OPR A-12	10.2	BHP A-11, RFT A-18	10.3
GPR A-12	8.13	WPR A-20, BHP A-08	9.71
BHP A-18	7.82	BHP A-07, RFT A-18	9.49

In the table, we use the notation GPR for gas production rate, WPR for water production rate, and OPR for oil production rate. Other symbols are defined above
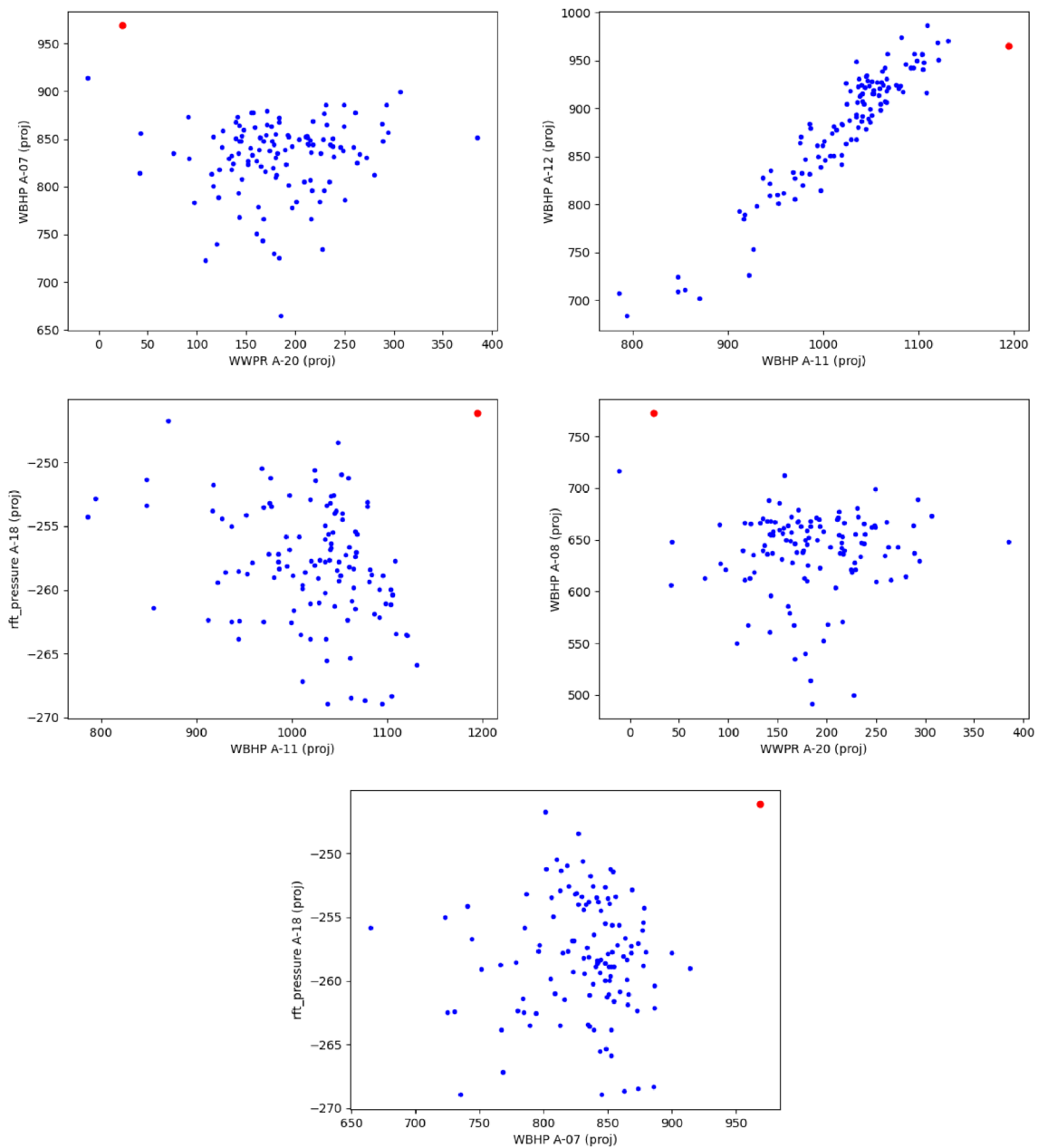
Fig. 13 Crossplots for data pairs with highest squared Mahalanobis distance score [dimensionless]. The blue dots are projected ensemble members and the red dot is the projected measurement

areas with negative changes in porosity for both datatypes. A challenge when working with imperfect models is that the lack of model complexity makes it impossible to match all data. This can be seen as a contradicting contribution from different data types on reservoir properties. However, if we filter the positive porosity gain from seismic on the areas where the porosity gain from oil production is negative (bottom plot), it reveals that there are very few inconsistent grid cells (i.e., cells where contributions from the two data types contradict).

5.2.2 Data match

Although the well data is not the primary focus of this paper, it is a challenge to simultaneously reduce the data mismatch for both seismic and well data. Scaling [19] of the two datatypes
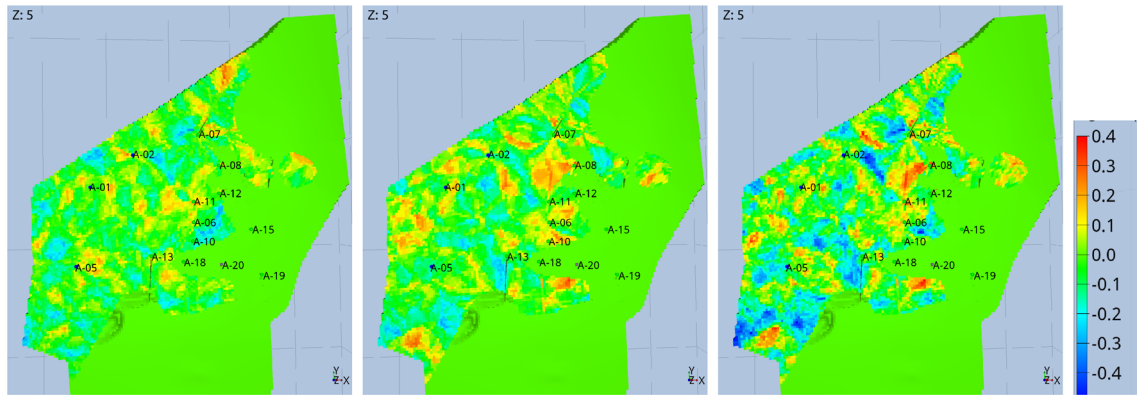
Fig. 14 Change in reservoir top parameter (see Table 2) induced by bottom hole pressure in injector A-01 (*left*) and producer A-12 (*middle*). The rightmost plot shows the sum of the two contributions. The update is based on the first iteration. [meters.]

is an efficient way of ensuring this. In this study, we used a scaling (or weighting) factor of 0.5. The average data match is computed using the formula

$$J^i = \frac{1}{N_d} \frac{1}{N_e} \sum_{j=1}^{N} \|d^o - d_j^i\|_{C_d^{-1}}^2, \qquad (15)$$

where i is the iteration index, N_e is the ensemble size, N_d is the number of data, and C_d is the data variance. The results are shown in Fig. 16. The well data approached the noise level after three iterations and the seismic data mismatch was

reduced by approximately 50 %. The reduction in the seismic data mismatch indicates a clear improvement to the model but also reveals that additional modifications of the prior model or the ensemble smoother configurations are required to further reduce the data mismatch.

The changes in prior and posterior amplitude maps for the two datasets are shown in Figs. 17 and 18 shows the difference between the posterior simulated amplitude mean and the field data. The first dataset is the difference between the 2018 monitor and the 2016 base survey, and the second dataset is the difference between the 2020 monitor and the 2018 survey. The second dataset (bottom) reveals a large area without sig-
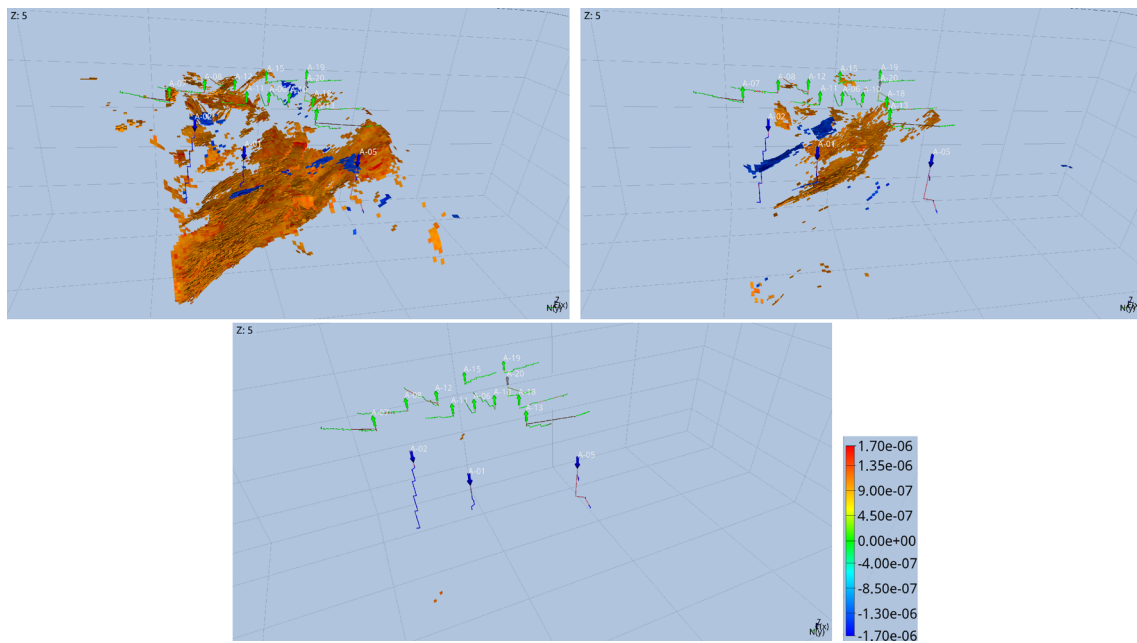
Fig. 15 Change in porosity [m³/m³] induced by seismic data (*left*) and oil production at A-11 (*right*). The bottom plot shows the positive change from seismic filtered on negative change from oil production. The updates are based on the first iteration. Injectors are shown as blue arrows, and producers are shown as green arrows. The colorbar applies to all plots
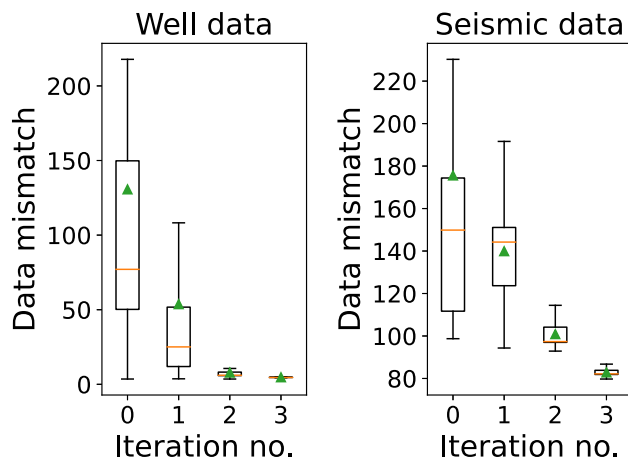
Fig. 16 Objective function for well data (production data, pressures, and RFT data) and seismic data. The box plots show the range, quartiles, mean (triangle), and median (orange line). Since the squared data are scaled by the variance (Eq. 15), there are no units on the axes

adjustments are in accordance with the assimilated seismic and well measurements, which indicate a successful update of the parameters. The main contribution from the updated parameters is the reduction of the waterfront displacement. This is achieved by increasing the porosity in the upper layers and by reducing the permeability in the direction between injectors and producers. This is discussed further in subsequent sections. Although clear improvements in the predicted amplitude are obtained, the results also reveal that the simulated data are still overly dispersed compared to the actual data. Ways to further improve the results will be a topic for future research.

The production data mismatch is reduced for most of the wells. A major contribution to this comes from uncertainty reduction (increased precision) for the updated ensemble. We assimilate data from the beginning of production (green field), and only small amounts of water are produced. The general trend is that less water is simulated compared to the measured values. In addition, the reservoir is under-saturated, so the produced gas is coming out of solution as a consequence of the pressure drop in the production tubings. These conditions make the reference model relatively good for the prediction of production rates. However, the reference pressure is poorly estimated for several of the wells. The updated ensemble is only partially able to improve the pressure data mismatch. Figure 19 shows production data for well A-18. The uncertainty for the data is reduced for both oil and water rates, and we obtain a slight increase in simulated water,

nal, which is caused by marine restrictions in the vicinity of the Edvard Grieg platform during data acquisitions. The first dataset clearly shows a shift towards the east for the simulated prior. A significant adjustment is then seen for the difference between the initial and final simulated data (see the right-most plot). The color scale shows a difference of magnitude around 0.4. The second dataset is considerably weaker, but also here there is an adjustment (reduction) in the east and an increase in signal strength in the middle west region. All

Fig. 17 Mean of simulated prior ensemble (*left*), mean of simulated posterior ensemble (*middle*), and the difference between the prior and posterior results (*right*). The right plots only show differences larger than 0.01. *Top*: Dataset based on 2018-2016 difference; *Bottom*: Dataset based on 2020-2018 difference

Fig. 18 Maps from averaging absolute field amplitudes in a window from 50 ms above to 50 ms below the reservoir top (*left*), and the difference between field data and the posterior results (*right*). The right plots only show differences larger than 0.01. *Top*: Dataset based on 2018-2016 difference; *Bottom*: Dataset based on 2020-2018 difference
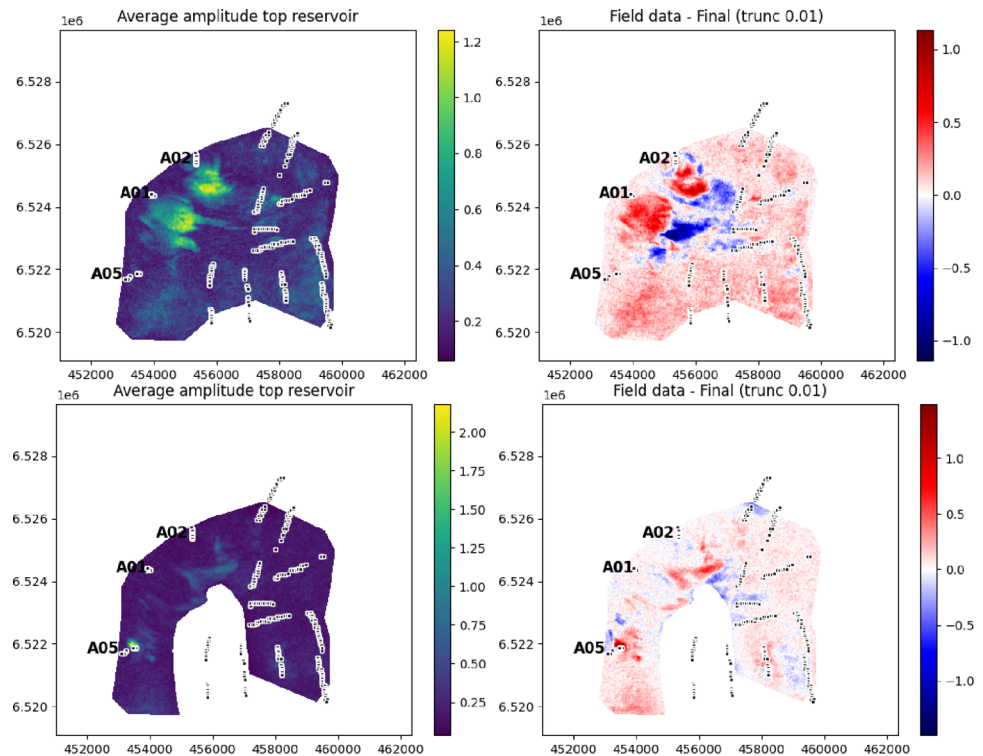
which is in accordance with the data. The bottom hole pressures for injector A-02 and producer A-10 are shown in Fig. 20. For the injector, we are underestimating the pressure, and only a small shift toward the data is obtained after data assimilation. Our ambition was to achieve a better match for the pressures by including uncertainty for the well production/injection indices, but in this case, the injection index is only marginally modified. The reason for this is that the automatic data noise inflation (mentioned in the first paragraph

of this section) has reduced the impact of the pressure data. The inflation of this data type should therefore be reduced or removed. This will be subject to further research in subsequent works. The pressure data for well A-10 is an example of a well with a good data match using the reference model, and in this case, the updated ensemble has low uncertainty and is centered between the measurements.

The RFT data match is also improved for most of the wells, and the uncertainty in the updated ensemble is reduced.
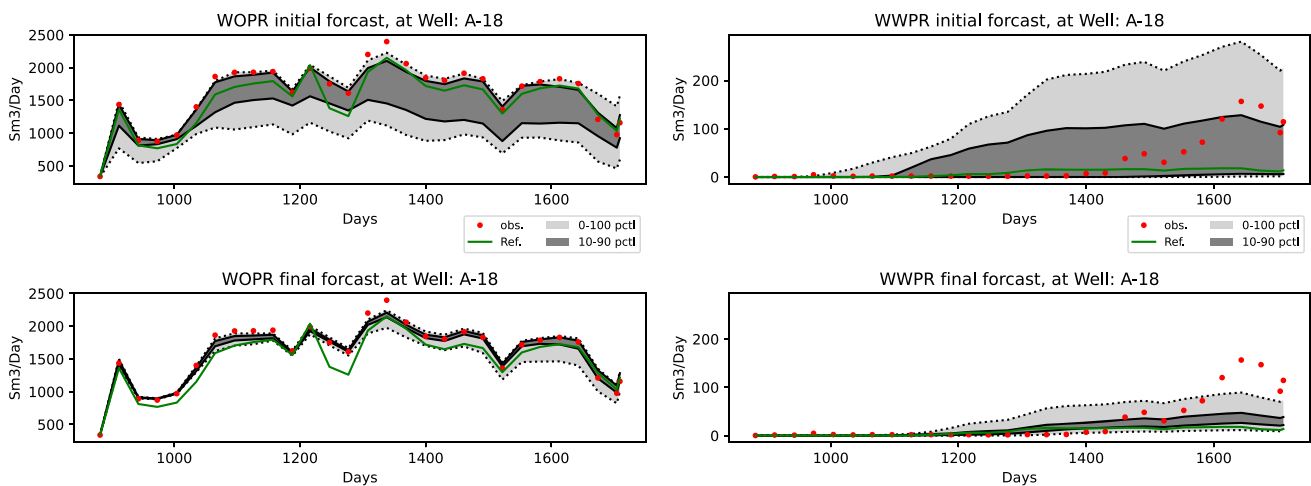
Fig. 19 Oil (*left*) and water (*right*) production rates at well A-18. The red dots are the measurements, the green line is the result using the reference model, the light gray domain indicates the spread of the ensemble,

and the dark gray indicates the 10th and 90th percentile for the ensemble. Day 0 on the x-axis is production start-up in November 2015
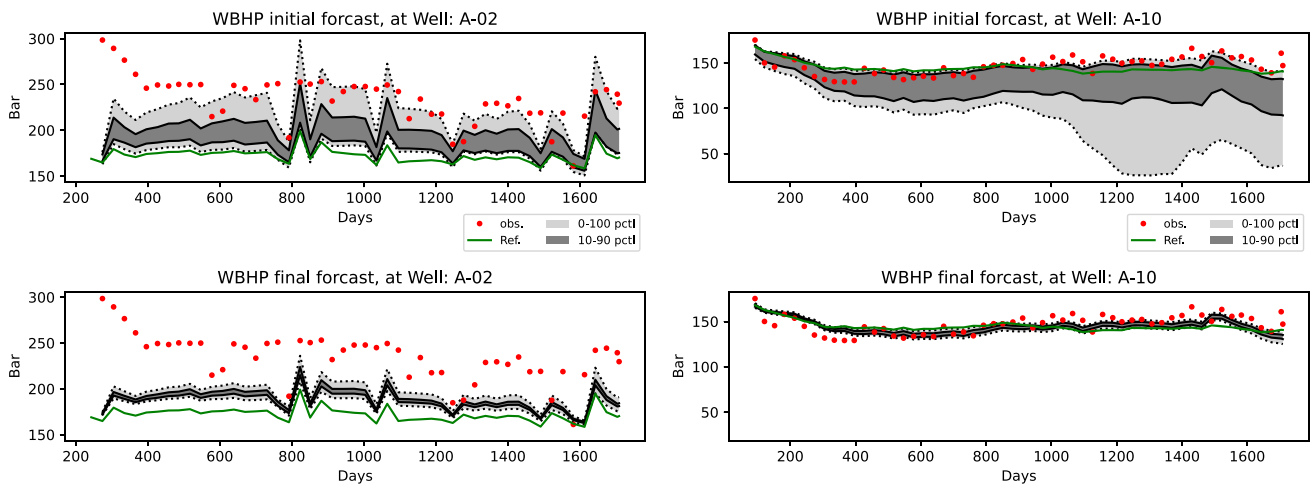
Fig. 20 Bottom hole pressure for injector A-02 (*left*) and producer A-10 (*right*).The red dots are the measurements, the green line is the result using the reference model, the light gray domain indicates the spread of the ensemble, and the dark gray indicates the 10th and 90th percentile for the ensemble. Day 0 on the x-axis is production start-up in November 2015

Figure 21 shows two examples of this for well A-08 and well A-12. The updated ensemble is mostly centered around its prior mean values, but for some of the data values the ensemble is also slightly shifted toward the measurement.

5.2.3 Estimated parameters and dynamic variables

The dynamic variables are not directly updated as part of the Bayesian inversion. It is however interesting to see the impact updated static parameters have on the reservoir flow, and in particular the saturation and pressure. The volume average of the change in water saturation is computed using the formula

$$\Delta S^w = \frac{1}{V^p} \sum_k \Delta S_k^w \cdot V_k^p, \tag{16}$$

where $\Delta S^w = S_i^w - S_{i-1}^w$ and V^p is the pore volume. The subscript i indicates the point in time for a seismic survey. The average is computed for each column in the reservoir model, and the summation index (k) is selected such that the total depth is approximately 100 meters, i.e., $L = \sum_k \Delta Z_k \approx 100$ m, where Z_k is the cell thickness. Figure 22 (left) shows the difference between posterior and prior ΔS^w. The first plot corresponds to the first amplitude dataset, and a clear delay of the water movement is indicated by the blue color. Erroneous water displacement is the main reason for the discrepancies between the measured signal and the simulated observations (Fig. 17). A further correction of the water displacement is seen on the second plot, which corresponds to the second dataset. Here the red color indicates that water is replacing oil in the posterior model, and the waterfront is precisely located at the transition between red and blue on the plot. Similar to
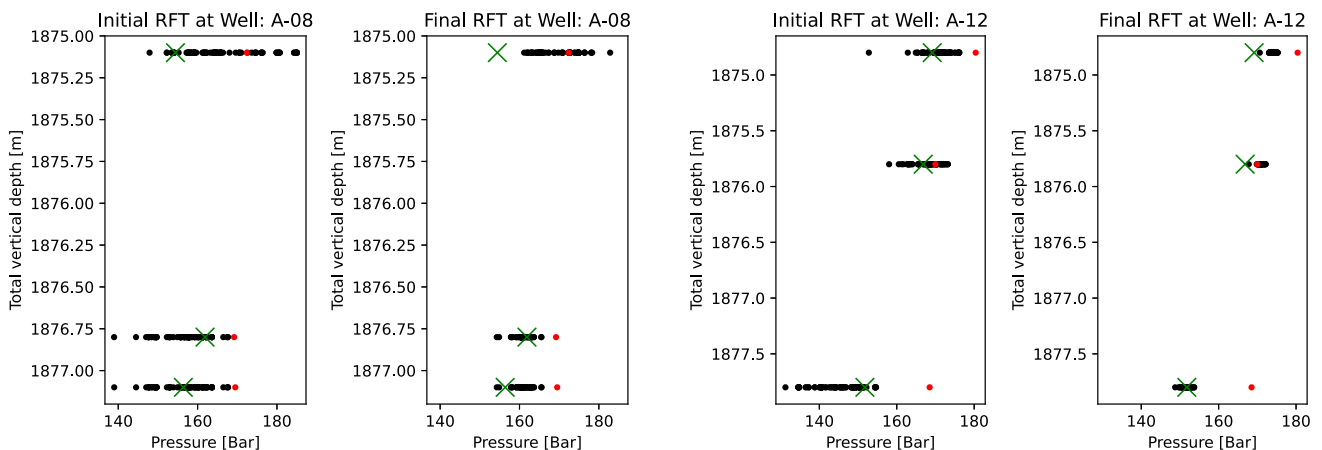
Fig. 21 RFT data for well A-08 (*left*) and A-12 (*right*). The red dots are the measurements, the green cross is the result using the reference model, and the black dots are the ensemble members

Fig. 22 *Left*: Difference between posterior and prior ΔS^w where ΔS^w is saturation change between the first monitor survey and the base survey (*top*), and between the second monitor survey and the first monitor survey (*bottom*) [percent]. *Right*: Difference between posterior and prior ΔP where ΔP is pressure change between the first monitor survey and the base survey (*top*), and between the second monitor survey and the first monitor survey (*bottom*) [bar]. The truncation values are shown in the titles. All quantities are based on volume averages
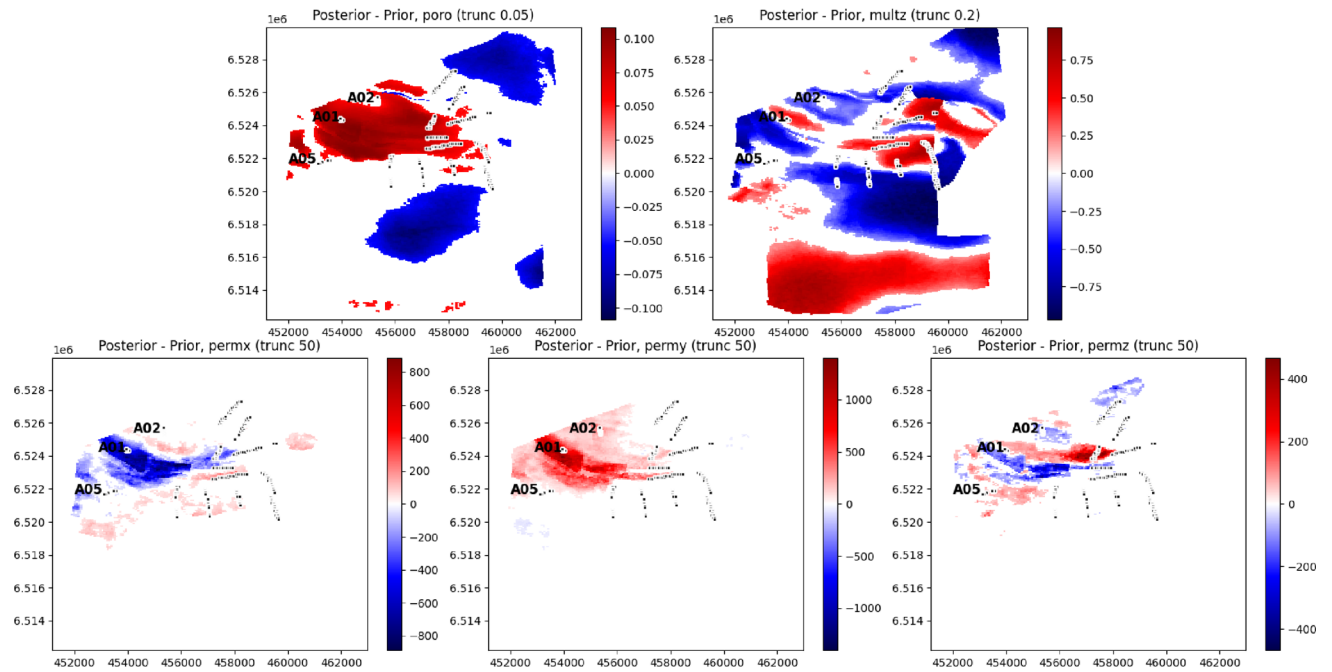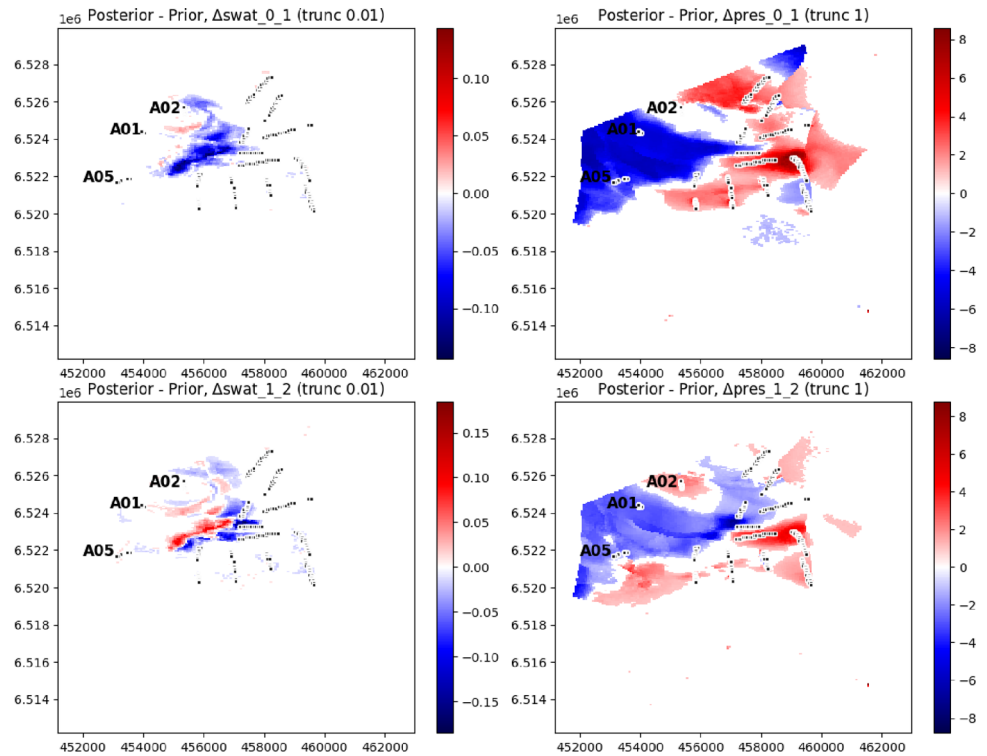
Fig. 23 *Top*: Difference between posterior and prior porosity (*left*) [m³/m³], and vertical permeability multiplier (*right*) [dimensionless]. *Bottom*: Difference between posterior and prior permeabilities in x (*left*), y (*middle*) and z (*right*) directions [mD]. The truncation values are shown in the titles. All quantities are based on volume averages

saturation, Fig. 22 (right) shows the volume averaged difference between posterior and prior pressure. For the Edvard Grieg field, there is an increase in pressure (over time) around the injectors in the west and a decrease in pressure (over time) around the producers in the east. The difference between the posterior and prior pressure maps reveals that these trends are flattened, i.e., the overall pressure changes in the reservoir are reduced over time. The governing explanation for this is the increased porosity between the injectors and producers, see Fig. 23 (top, left). An exception is an area around injector A-02, where the porosity is approximately kept unchanged. The increase in porosity between the injectors and producers slows down the water movement, which is one of the major contributions to a better match between measured and simulated amplitude maps. The decrease in porosity in the north and south can be a consequence of the correlated porosity fields that are used for the prior ensemble, or it could be related to spurious correlations that are not eliminated by the localization. It could also be other physical explanations related to pressure or water movement. As discussed in the preliminary study, it is likely that the vertical connectivity should be reduced in the vicinity of injector A-02, which is confirmed by the blue area around this well, see Fig. 23 (top, right). The overall modifications of the multipliers are however quite complex and consist of both increase and decrease at different parts of the reservoir. For instance, there is a significant reduction of the vertical permeability multiplier between injectors A-01 and A-05, and around producers A-13 and A-18. There is an increase in the vertical permeability multiplier north of injector A-02, around producer A-10, and in the southern part of the reservoir. However, reduced connectivity around injector A-02 is strengthened by a reduction in vertical permeability, seen in Fig. 23 (bottom, right). The decrease of x-permeability, Fig. 23 (bottom, left), contributes to slowing down the water movement between the injectors and producers. Similarly, and the increase in y-permeability, Fig. 23 (bottom, middle), contributes to a redirection of the water movement towards the flanks of the reservoir.

The change in reservoir top depth is shown in Fig. 24 (right). Positive change means that the top is lower and the oil column is reduced, and vice versa. It is a decrease in the reservoir top east of injectors A-01 and A-05, that contributes to higher (vertically averaged) water saturation in this area. However, as mentioned in the section about model checking, the main contribution to changing the reservoir top comes from the pressure data. Due to relatively moderate changes in the top depth, we decided to increase the uncertainty in the top depth in future simulations, as two meters standard deviation may be too small to gain a significant impact on the flow. The prior and posterior standard deviations for the depth parameter are shown on the left and middle plots, respectively. The conditioning on well depths is seen as domains with zero standard deviations.

In Fig. 25 we show a selection of scalar parameters with large differences between the prior and posterior ensemble. For the water contacts, the general trend among the posterior distributions is to lower the contact and increase the thickness of the oil column. Most change is seen for equilibrium zone 3 (see also Fig. 5) where the average change is almost two meters. Regarding relative permeabilities, the largest update is seen for the gas phase, which is lowered by approximately 0.2. This has an impact on the movement of gas that evaporates (comes out of solution) due to pressure drop around the producers. Finally, we have included the results for the pore volume multiplier. For this parameter, we selected a prior mean of 2, and the updated mean is almost 2.75. The purpose of adding uncertainty to the pore volume is to allow variation of the pressure support from the aquifer, which is strengthened in the posterior model.

Figure 26 shows prior and posterior distributions for three (out of 17 in total) fault multipliers. These faults all change significantly compared to the prior values, and the posterior distributions all suggest less transmissibility, close to sealing. The position of the faults is shown in Fig. 27. The first gravitational fault acts as a barrier between injectors A-01 and A-02 and producers A-13 and A-18, and will impact the
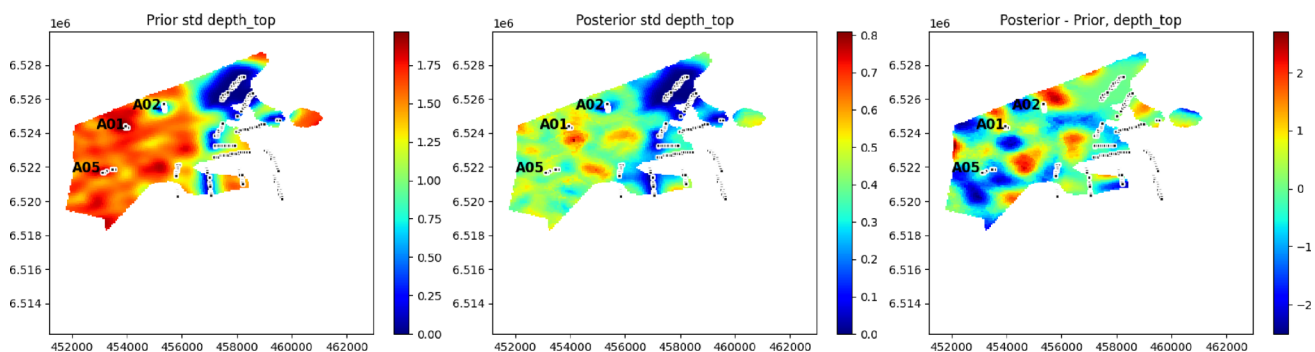
Fig. 24 Differences between posterior and prior reservoir top depth (*left*), prior (*middle*) standard deviations, and posterior (*right*) standard deviations. [meters.]
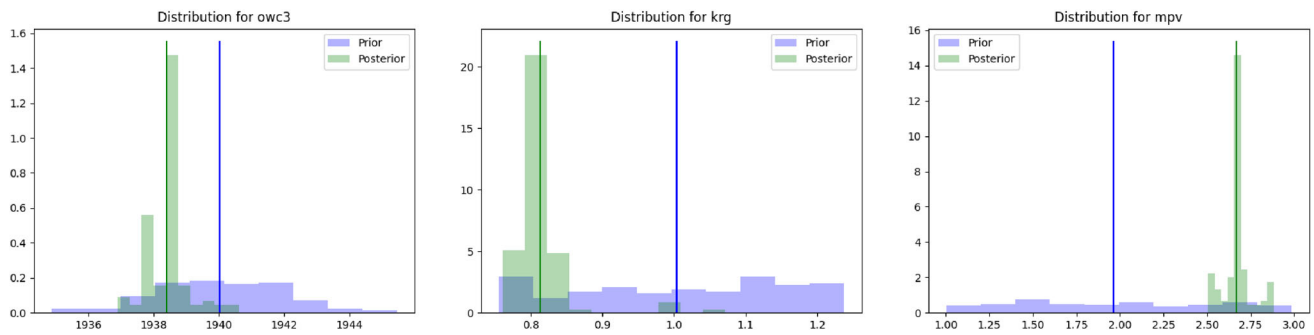
Fig. 25 Oil-water contact for equilibrium zone 3 (*left*) [unit x-axis meters], relative gas permeability (*middle*) [dimensionless], and pore volume multiplier (*right*) [dimensionless]. The y-axis shows the probability density

water movement in this direction and the production data for the wells. The fault in the southwest is close to injector A-05, and acts as a support for directing the water toward the east. The Tellus fault is located north of producers A-07 and A-08 and less transmissibility for this fault is likely to impact the pressure around these wells.

5.2.4 Model validation

As part of the posterior model validation, we compute different statistical measures. The first measure is how much the standard deviation changes for a parameter or parameter group (by parameter group we mean cell-based parameters such as porosity or the reservoir top depth). This measure is useful to check that the ensemble does not collapse (zero standard deviation), but also to verify that the uncertainty is actually reduced. The second measure is how much the posterior parameters change compared to the prior values. Generally, it is unwanted to move too far from the prior values as this may imply geological structures that are not credible or physical. In order to measure this we compute the percentage of parameters in a group that has their posterior mean value more than one, two, and three prior standard deviations away from the prior mean value. For scalar parameters, the measure is simply if this parameter changes more

than one, two, or three prior standard deviations compared to the prior value. Table 4 summarizes the measures for the parameter groups and the scalar parameters that change more than one prior standard deviation. Firstly, we can conclude that the ensemble has not collapsed for this run. Secondly, a moderate percentage of the parameters in the groups change more than one standard deviation, and a very small number of parameters change more than two standard deviations. No parameters change more than three standard deviations. None of the scalar parameters change more than one standard deviation. In our opinion, these numbers are within a reasonable range. In particular, it is important to limit the updates of porosity, since the prior information is relatively accurate in the vicinity of the wells.

For further inspection, we have implemented the possibility to export (as .grdecl files) the amount of change for grid-based parameters. Figure 28 shows the change in porosity and x-permeability. As expected, the majority of change occurs in the center of the reservoir that covers the wells.

5.3 Assimilating impedance cubes

In this section, we present results using 3D acoustic impedance (I_p) cubes, and similar to amplitude maps, two datasets are generated based on the difference between the first monitor
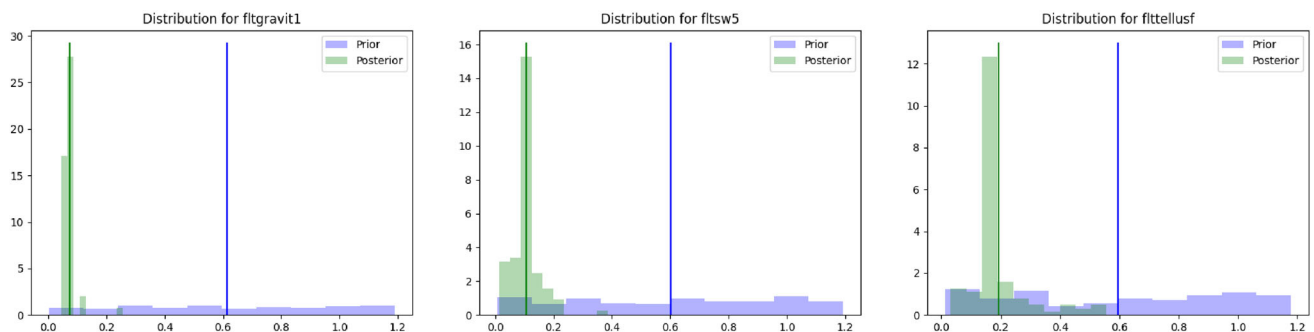
Fig. 26 Transmissibility multipliers for the first gravitational fault (*left*) [dimensionless], the fifth southwest fault (*middle*) [dimensionless], and the Tellus fault (*right*) [dimensionless]. The y-axis shows the probability density

Fig. 27 The faults sw5, gravit1, and tellusf (shown in pink) visualized on top of the difference between posterior and prior ΔS^w where ΔS^w is saturation change between the first monitor survey and the base survey [percent]
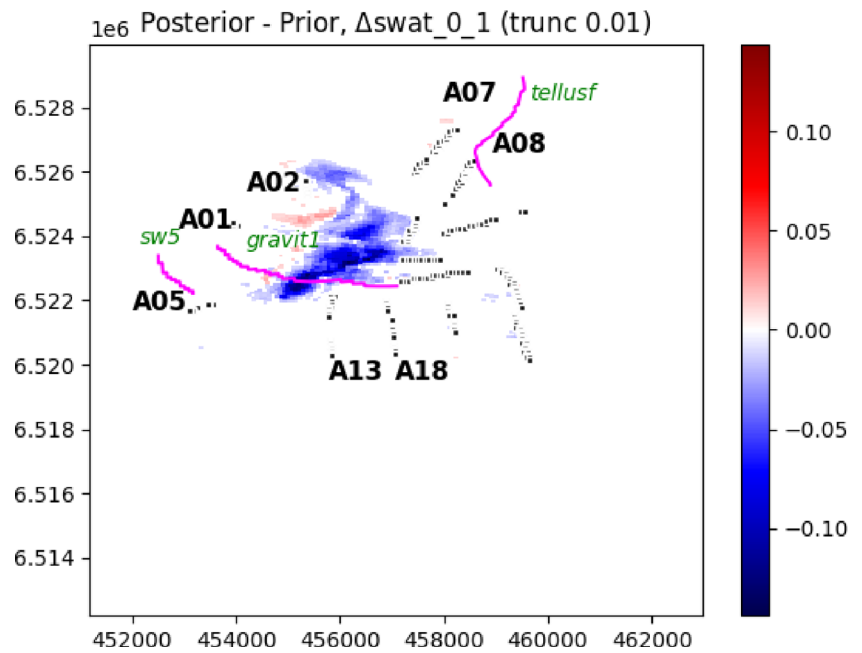
survey and the base, and the difference between the second monitor survey and the first monitor survey. The cubes are represented in the seismic domain (see Section 3.2.2), and the two datasets have original sizes of 58736259 and 47914645 numbers, respectively. Before assimilation, the data is compressed using the methodology described in Section 4.4, and the reduced sizes are 33886 and 52001 numbers, which corresponds to compression of 99.94% and 99.89%. Figure 29 shows the first data set without any compression and the corresponding reconstructed dataset after compression. Visually, it is only minor differences between the two versions of the dataset. In order to avoid different scales for simulated and

field data, each dataset is scaled using the 99.99 percentile value for the dataset.

We made some adjustments to the setup of the assimilation methodology in this case. The damping factor is increased to $\lambda_0 = 1 \cdot 10^7$ (see Section 4.2) in order to force smaller update steps. This adjustment was necessary to achieve a proper decrease in the data mismatch during iterations. We also reduced the localization truncation scaling to $\tau = 0.5$ (see Section 4.3), in order to make sure that all parameters with correlations to the data are included when updating the models. Furthermore, because of the compression of the seismic data, the prior mismatch for seismic data is of a similar

Table 4 Change in standard deviations and mean values

Parameter	Prior std	Posterior std	$> 1\sigma_p$	$> 2\sigma_p$	$> 3\sigma_p$
Top depth	1.24	0.35	17.3	0.13	0.
Log-perm x	0.20	0.06	16.2	0.08	0.
Log-perm y	0.20	0.06	16.2	0.70	0.
Log-perm z	0.20	0.06	14.9	0.24	0.
Multz	1.00	0.27	20.6	0.22	0.
Porosity	0.06	0.02	26.4	0.13	0.
Multpv	1.03	0.18	✓	−	−
Krg	1.01	0.32	✓	−	−
Log-WPI A-07	0.99	0.37	✓	−	−
Multflt sw4	1.00	0.31	✓	−	−
Multflt sw5	1.01	0.24	✓	−	−
Multflt gravitat	1.03	0.30	✓	−	−
Multflt gravit1	1.03	0.13	✓	−	−

Here multipliers for pore volume and faults are denoted 'Multpv' and 'Multflt', respectively. Relative permeability for gas is denoted 'Krg'
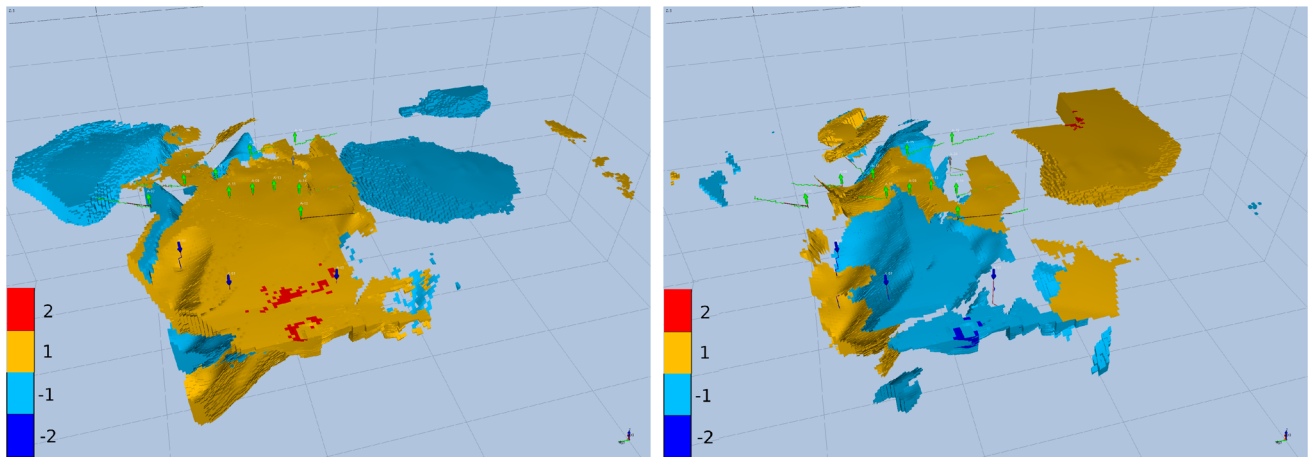
Fig. 28 Amount of change for porosity [m³/m³] (*left*) and x-permeability [mD] (*right*). The colors indicate more than two standard deviations in positive direction (red), more than one standard deviation in positive direction (orange), more than two standard deviations in negative direction (blue), and more than one standard deviation in negative direction (light blue)
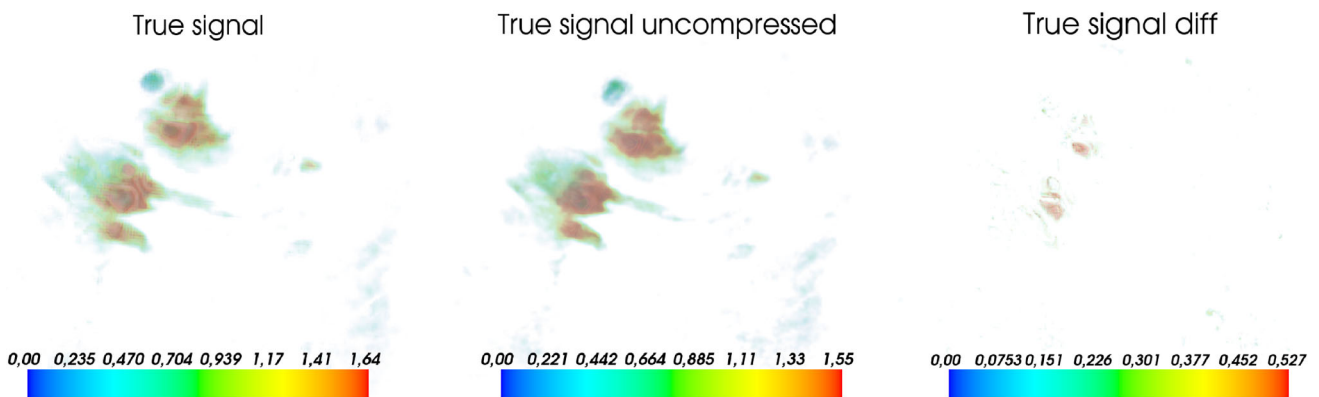

Fig. 29 Volume view of impedance. Visualization of the first dataset (difference between first monitor survey and base survey) for field data without compression (*left*), with compression (*middle*), and the difference (*right*). The data are scaled and therefore dimensionless

Table 5 Mean, standard deviation, minimum, and maximum for the prior ensemble

Parameter type	mean (μ)	std (σ)	min	max
Top	μ_{ref}	5		
Porosity	$\bar{\mu}_{\text{ref}}$	0.0625	0	1
Net-To-Gross (NTG)	$\bar{\mu}_{\text{ref}}$	0.0625	0	1
Log-permeability (x, y, z)	$\log(\bar{\mu}_{\text{ref}}) - \sigma^2/2$	0.3	-5	10
Multz (cfd)	0	1	0	2
OWC	μ_{ref}	3		
Log-WPI	$0 - \sigma^2/2$	1		
Kr (w,o,g) (cfd)	0	1	0.75	1.25
Multpv (cfd)	0	1	1	10
Multflt (cfd)	0	1	0	1.2

The blue color indicates changes compared to the previous case using amplitude maps. The bar over μ indicates that the mean is computed as the average of reference values for each facies type. For spatially distributed parameters, a variogram range of 40 gridblocks (in all directions) is used
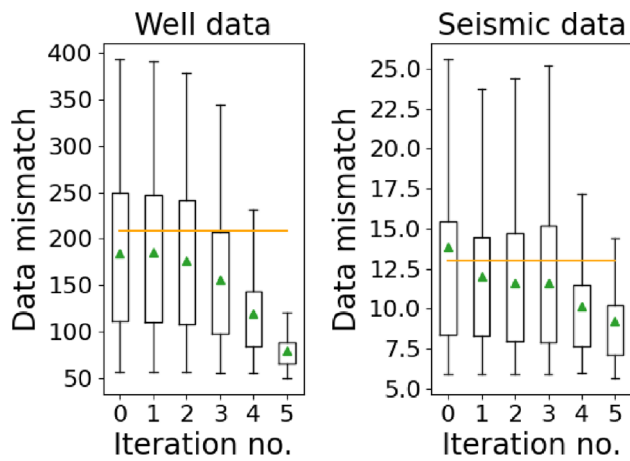
Fig. 30 Objective function for well data (production data, pressures, and RFT data) and seismic data. The box plots show the range, quartiles, and mean (triangle). The orange line represents the average reference data mismatch

magnitude as the prior mismatch of production data. We can therefore omit the scaling factor between seismic and production data in this case.

We also did some modifications to the setup of the prior ensemble in this case. The major change is that the mean of the ensemble is now based on the mean of the reference parameters, evaluated in each facies type. I.e., we first compute the mean of the reference fields for each facies type and then use the calculated values as the mean for the Gaussian distribution we use to generate the prior ensemble. In addition, we have extended the span of the parameter representing the top reservoir. In the previous case, the parameter represented the interface between the chalk and sand facies. Now the parameter represents the interface between the chalk and all facies types (i.e., both sand and conglomerate). We also included the Net-To-Gross in this study, and we have increased the uncertainty for some of the parameter types, thereby achieving a broader search space for the updated models. The values used for generating the prior ensemble are summarized in Table 5.

The data mismatch for well and seismic data is shown in Fig. 30. Since the information contained in the reference model is mostly ignored in this case, we decided to compare the calculated prior data mismatch with the cor-
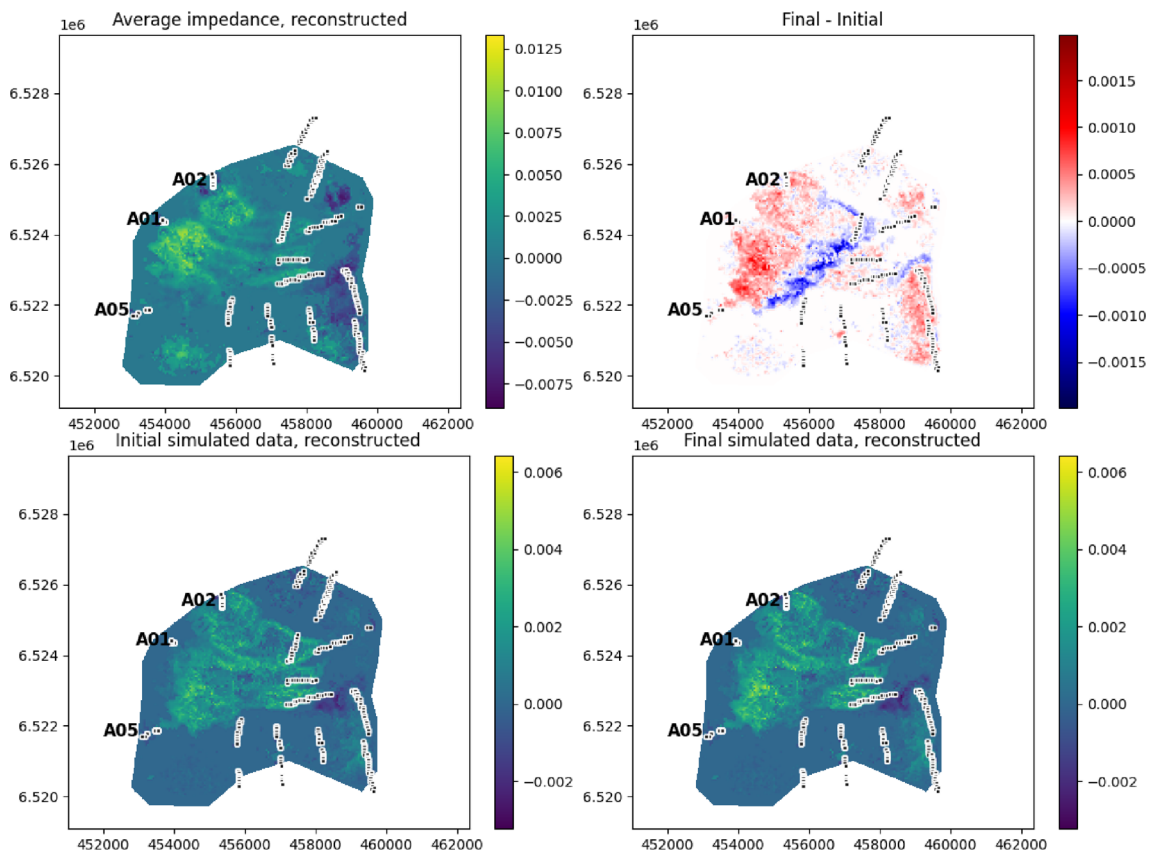
Fig. 31 Vertically averaged maps of scaled impedance. Visualization of the first dataset (difference between first monitor survey and base survey) for field data (*top left*), prior simulated data (*bottom left*), posterior simulated data (*bottom right*), and the difference between the final simulated data and the initial simulated data (*top right*). The data are scaled using the 99.99 percentile value for the dataset, and therefore dimensionless
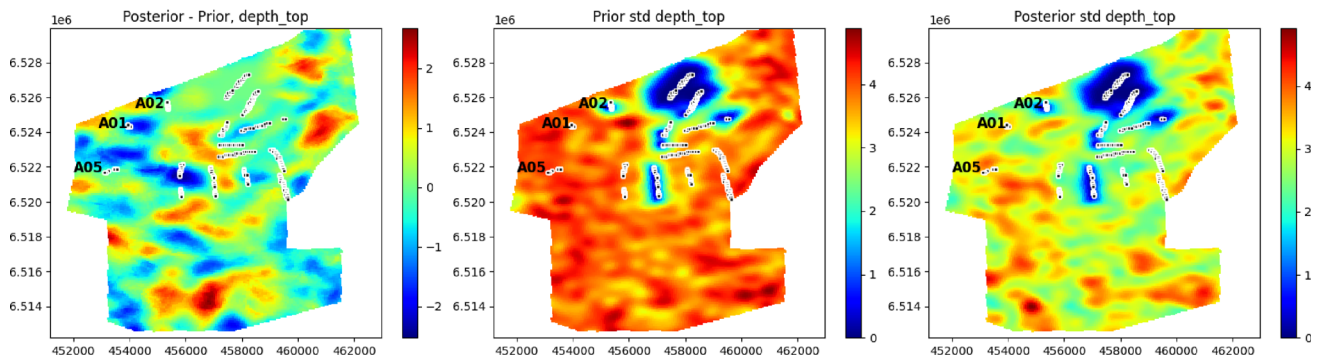
Fig. 32 Differences between posterior and prior reservoir top depth (*left*), prior (*middle*) standard deviations, and posterior (*right*) standard deviations. [meters.]

responding values obtained using the reference model. The data mismatch for the reference model is computed based on a forecast using an ensemble with identical statistics as listed in Table 5, except that the mean values are reference fields without any averaging. Also, the random seed is identical when generating ensembles with and without averaged reference values. A Forecast of a full ensemble is required for the reference model since the data compression depends on the simulated ensemble (see also Section 4.4). The figure shows that the data mismatch decreases for each iteration and the final updated model achieves a lower mismatch compared to the reference case.

We will focus on the seismic data in this section, as the data match for production data is similar to the previous case. Also, the Mahalanobis measures are of a similar magnitude as before. Figure 31 shows the first dataset based on inverted seismic measurements and prior and posterior simulated observations. We have computed an average of the data over the vertical direction. As for the amplitude maps, the differences in prior and posterior datasets are visually enhanced by plotting the difference using a cold/warm colormap. As before, the main contribution to the improved data match is the sharpening of the waterfront, seen as a reduction of the signal ahead of the front and an increase of the signal behind

the front. A similar conclusion can be drawn for the second dataset and to limit the length of the paper we omit the figures for this. As mentioned at the beginning of this section, we used small update steps for the iterative smoother when assimilating impedance data. The consequence is smaller changes in the model, compared to the case using amplitude maps. However, it is likely that we can achieve a higher reduction in the data mismatch by adjusting the damping factor and the adaptive rules for updating the factor. In the conclusion section, we discuss other possibilities for improving the model.

Figure 32 shows the estimated change in the reservoir top and the corresponding change in standard deviations. Notice the extended spatial domain for the depth, compared to the previous case. Similar to the previous case, we see a decrease in the top depth east of the injectors. As this has a direct impact on the connectivity in the high-permeability zone, the reduction of the top depth influences the reservoir pressure and thereby also the simulated impedance. The standard deviation for this parameter is reduced, but for most of the domain (except around the wells) the posterior standard deviation is above 2 meters.

Finally, in Fig. 33 we show the change in volume averaged porosity and the corresponding prior and posterior parame-
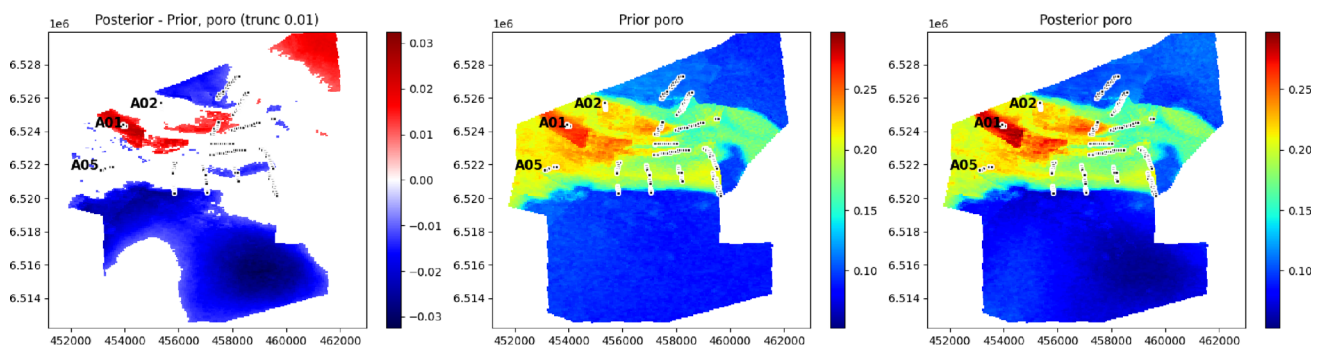
Fig. 33 Differences between volume averaged posterior and prior porosity (*left*), prior (*middle*) standard deviations, and posterior (*right*) standard deviations. [m^3/m^3.]

ter fields. The increase in porosity east of injector A-01 is the main driver for waterfront displacement and contributes to improved data match. There are also significant changes in porosity further away from the wells, which may be a consequence of the spatial correlations imposed on the prior porosity fields.

6 Conclusion

The primary objective of this study is to demonstrate a functional workflow for assimilating large datasets (seismic attributes) into complex reservoir models and to demonstrate the results for the Edvard Grieg field. Here, a novel approximation of the combined Kirchhoff modeling and imaging operator known as the point spread function is implemented and multi-scale models for simulating seismic data are presented. Further, we use a new compression technique for handling large datasets. We have demonstrated the use of several new methods and visualization techniques for model creation, model checking, and model validation, which is essential for an efficient workflow. In particular, new methods for checking the coverage of simulated data are introduced, and we demonstrate the use of the Mahalanobis distance to evaluate the credibility of the prior ensemble. We also show how ranking of data based on their impact on the reservoir properties, and visualization of the changes induced by the most influential data, can provide valuable insight into model deficiencies. We also check if data are giving contradicting contributions to the reservoir properties, and if model imperfections imply that additional parameters need to be included in the workflow. These techniques allowed us to improve the model and form a foundation for parameter selection, even before executing the Bayesian inversion. After history matching the reservoir, we computed statistical measures for validating the updated ensemble and checking that ensemble collapse is avoided.

Posterior results show that we can reduce the data mismatch for both well data and seismic data. Of particular interest is the fact that calibrated models are better at predicting water displacement. The combination of seismic data and the iterative ensemble smoother results in a modified reservoir model with different pore volumes and STOOIP (stock tank original oil in place), which alters the water movement and adjusts the seismic response in agreement with the data. This was achieved without contradicting the well logs and direct observations of reservoir properties. Consistent results are obtained based on two different seismic attributes, namely average amplitude maps and scaled impedance cubes, and the updates for the reservoir properties are in accordance with the operators' geological understanding of the field.

The seismic data mismatch is reduced by approximately 50 % in our study. The obtained values are not yet at the theoretical limit (the limit is unity when using the data mismatch formula described in this paper), which indicates room for improvement. As demonstrated in e.g., [27], validation of results from the posterior model, after running the Bayesian workflow, may reveal that parameters (e.g., fault multipliers or water-oil contacts) are missing in the model. A successful calibration then requires model improvement (i.e., identification and inclusion of missing parameters) before running the workflow again. The inclusion of the top surface of the reservoir was a consequence of this approach, and this parameter accounts for structural uncertainty in the model updating part. However, in our case, we may be required to include additional structural parameters describing the geological model in the set of prior uncertain parameters. This will be a topic for future research. Since the specification of correlated measurement errors is difficult, we also want to pursue an alternative approach that integrates out the measurement errors, as described in [30]. In addition, the study revealed a need for faster models targeted for data assimilation, which enables the evaluation of different hyperparameters (e.g., settings for the inversion methodology) and data types. Multi-fidelity models (e.g., models with different levels of upscaling) are already being investigated, and the use of these models for fast and efficient large-scale data assimilation will be a prioritized task in the future.

Declarations

References

1. Avseth, P., Skjei, N.: Rock physics modeling of static and dynamic reservoir properties—a heuristic approach for cemented sandstone reservoirs. Lead. Edge. **30**(1), 90–96 (2011). https://doi.org/10.1190/1.3535437

2. Avseth, P., Dvorkin, J., Mavko, G., et al.: Rock physics diagnostic of North Sea Sands: Link between microstructure and seismic properties. Geophys. Res. Lett. **27**(17), 2761–2764 (2000). https://doi.org/10.1029/1999GL008468

3. Avseth, P., Johansen, T.A., Bakhorji, A., et al.: Rock-physics modeling guided by depositional and burial history in low-to-intermediate-porosity sandstones. Geophysics **79**(2), D115–D121 (2014). https://doi.org/10.1190/geo2013-0226.1

4. Ceetron Solutions (2022) Resinsight. https://resinsight.org

5. Chen, Y., Oliver, D.S.: Ensemble randomized maximum likelihood method as an iterative ensemble smoother. Math. Geosci. **44**(1), 1–26 (2012). https://doi.org/10.1007/s11004-011-9376-z

6. Chen, Y., Oliver, D.S.: Levenberg-marquardt forms of the iterative ensemble smoother for efficient history matching and uncertainty quantification. Comput. Geosci. **17**(4), 689–703 (2013). https://doi.org/10.1007/s10596-013-9351-5

7. Chen, Y., Oliver, D.S.: History matching of the Norne full-field model with an iterative ensemble smoother. SPE Reserv. Eval. Eng. **17**(02), 244–256 (2014). SPE-164902-PA

8. Emerick, A.A.: Analysis of the performance of ensemble-based assimilation of production and seismic data. J. Pet. Sci. Eng. **139**, 219–239 (2016). https://doi.org/10.1016/j.petrol.2016.01.029

9. Emerick, A.A., Reynolds, A.C.: Ensemble smoother with multiple data assimilation. Comput. Geosci. **55**, 3–15 (2013). https://doi.org/10.1016/j.cageo.2012.03.011

10. Evensen, G., Eikrem, K.S.: Conditioning reservoir models on rate data using ensemble smoothers. Comput. Geosci. **22**(5), 1251–1270 (2018). https://doi.org/10.1007/s10596-018-9750-8

11. Gazdag, J.: Wave equation migration with the phase-shift method. GEOPHYSICS **43**(7), 1342–1351 (1978). https://doi.org/10.1190/1.1440899

12. Gelman, A., Vehtari, A., Simpson, D., et al.: Bayesian workflow. (2020) arXiv:2011.01808, 2020

13. Golub, G.H., Van Loan, C.F.: Matrix Computations. Johns Hopkins series in the mathematical sciences, The Johns Hopkins University Press, Baltimore (1983)

14. Gu, Y., Oliver, D.S.: An iterative ensemble Kalman filter for multiphase fluid flow data assimilation. SPE J. **12**(4), 438–46 (2007). https://doi.org/10.2118/108438-PA

15. Leeuwenburgh, O., Meekes, S., Vandeweijer, V., et al.: Stochastic history matching to time-lapse seismic of a CO2-EOR project sector model. Int. J. Greenh. Gas Control **54**(2), 441–453 (2016). https://doi.org/10.1016/j.ijggc.2016.05.027

16. Lie, E.O., Bhakta, T., Sandø, I.: Seismic modeling using dual-reservoir and geophysical models. In: SEG International Exposition and Annual Meeting. (2021) https://doi.org/10.1190/segam2021-3583399.1

17. Lie, E.O., Bhakta, T., Sandø, I.: Inclusion of seismic attributes in reservoir ensemble coverage analysis. Lead. Edge **41**(12), 848–856 (2022). https://doi.org/10.1190/tle41120848.1

18. Lorentzen, R.J., Luo, X., Bhakta, T., et al.: History matching the full Norne field model using seismic and production data. SPE J. **24**(04), 1452–1467 (2019). https://doi.org/10.2118/194205-PA

19. Lorentzen, R.J., Bhakta, T., Grana, D., et al.: Simultaneous assimilation of production and seismic data: application to the Norne field. Comput. Geosci. **24**, 907–920 (2020). https://doi.org/10.1007/s10596-019-09900-0

20. Luo, X., Bhakta, T.: Automatic and adaptive localization for ensemble-based history matching. J. Petrol. Sci. Eng. 184(March 2019), 106559 (2020). https://doi.org/10.1016/j.petrol.2019.106559

21. Luo, X., Stordal, A.S., Lorentzen, R.J., et al.: Iterative ensemble smoother as an approximate solution to a regularized minimum-average-cost problem: Theory and applications. SPE J. **20**(5), 962–982 (2015). https://doi.org/10.2118/176023-PA

22. Luo, X., Bhakta, T., Jakobsen, M., et al.: Efficient big data assimilation through sparse representation: a 3D benchmark case study in petroleum engineering. PLOS ONE **13**, e0198586 (2018)

23. Luo, X., Lorentzen, R.J., Valestrand, R., et al.: Correlation-based adaptive localization for ensemble-based history matching: Applied to the Norne field case study. SPE Reserv. Eval. Eng. (2019) in press https://doi.org/10.2118/191305-PA, SPE-191305-PA

24. Mahmic, O., Dypvik, H., Hammer, E.: Diagenetic influence on reservoir quality evolution, examples from Triassic conglomerates/arenites in the Edvard Grieg field. Norwegian North Sea. Mar. Pet. Geol. **93**, 247–271 (2018)

25. da Nobrega, D.V., de Moraes, F.S., Emerick, A.A.: Data assimilation of a legacy 4D seismic in a brown field. J. Geophys. Eng. **15**(6), 2585–2601 (2018). https://doi.org/10.1088/1742-2140/aadd68

26. Norce Energy (2023) Python Ensemble Toolbox (PET). https://github.com/Python-Ensemble-Toolbox/PET, Data assimilation and optimization group

27. Oliver, D.S.: Diagnosing reservoir model deficiency for model improvement. J. Petrol. Sci. Eng. **193**, 107367 (2020). https://doi.org/10.1016/j.petrol.2020.107367

28. Oliver, D.S., Fossum, K., Bhakta, T., et al.: 4D seismic history matching. J. Pet. Sci. Eng. **207**, 109119 (2021). https://doi.org/10.1016/j.petrol.2021.109119

29. Rasmussen, A.F., Sandve, T.H., Bao, K., et al.: The open porous media flow reservoir simulator. Comput. Math. App. **81**, 159–185 (2021). https://doi.org/10.1016/j.camwa.2020.05.014, development and Application of Open-source Software for Problems with Numerical PDEs

30. Stordal, A., Lorentzen, R., Fossum, K.: Marginalized iterative ensemble smoothers for data assimilation. Comput. Geosci. (2023). https://doi.org/10.1007/s10596-023-10242-1

31. Walpole, L.J.: On bounds for the overall elastic moduli of inhomogeneous systems—I. J. Mech. Phys. Solids **14**(3), 151–162 (1966a). https://doi.org/10.1016/0022-5096(66)90035-4

32. Walpole, L.J.: On bounds for the overall elastic moduli of inhomogeneous systems—II. J. Mech. Phys. Solids **14**(5), 289–301 (1966b). https://doi.org/10.1016/0022-5096(66)90025-1

33. Yin, Z., Feng, T., MacBeth, C.: Fast assimilation of frequently acquired 4D seismic data for reservoir history matching. Comput. Geosci. **128**, 30–40 (2019). https://doi.org/10.1016/j.cageo.2019.04.001